Validation of ocean tide models around Antarctica using onshore GPS and gravity data

Matt King, Nigel Penna and Peter Clarke

School of Civil Engineering and Geosciences, University of Newcastle, Newcastle upon Tyne, NE1 7RU, United Kingdom

Ed King

Physical Sciences Division, British Antarctic Survey, Cambridge, CB3 0ET, United Kingdom

Abstract: Ocean tide models around Antarctica are presently only sparsely tested against independent data. Ocean tide modeling errors, along with subsequent ocean tide loading (OTL) displacement modeling errors, alias into altimetry and time variable gravity (e.g., GRACE) time series, for example. To validate various ocean tide models around Antarctica, GPS data from fifteen sites have been used to derive three-dimensional displacement estimates at eight diurnal and semidiurnal tidal frequencies. Using hundreds of days of GPS data, harmonic parameters were estimated on a daily basis then combined. These were then compared with OTL displacement estimates derived from global and regional ocean tide models. In East Antarctica, where the tides are well-defined, sub-millimeter differences are demonstrated in each coordinate component with the lunar N_2 and Q_1 constituents in closest agreement. As found in other studies, K_1, and especially K_2, agree less well. The spatial variation in the misfits for these two constituents indicates a site-dependency, with the K_2 errors also suggesting an interaction with satellite-dependent effects. In West Antarctica, where sites are nearer the largest ice shelves, agreement with the older models (CSR3 and TPXO.2) and NAO.99b is poor for all constituents. Modeled tidal gravity variations were also compared with gravity measurements at the South Pole. Overall the GPS and gravity data agree best with newer tide models, namely TPXO.6, CADA00.10, FES99 and

CATS02.01. However, validation data is lacking at the southern extents of the large ice shelves and hence some uncertainty still exists in all ocean tide models in these regions.

King, M. A., N. T. Penna, P. J. Clarke, and E. C. King (2005), Validation of ocean tide models around Antarctica using onshore GPS and gravity data,J. Geophys. Res., 110, B08401, doi:10.1029/2004JB003390.

1. Introduction

Satellite-based measurements in and across Antarctica are now routinely made for the purposes of crustal dynamics, post-glacial rebound, ice sheet mass balance, ice dynamics and water vapor studies, amongst others [*Anandakrishnan et al.*, 2003; *Dach and Dietrich*, 2001; *Dietrich et al.*, 2001; *Manson et al.*, 2000; *Tregoning et al.*, 2000; *Zwally et al.*, 2002]. If these measurements are to be of high precision and accuracy, the ocean tides and resulting displacement of the solid Earth due to ocean tide loading (OTL) must be accurately modeled. However, the ocean tides and resulting OTL displacements are some of the largest uncertainties in present-day satellite-based positioning and gravity field measurements. For example, aliased tidal signals in time-variable GRACE [*Tapley et al.*, 2004] gravity fields due to errors in current tide models may be more than one order of magnitude greater than the GRACE error budget in the Antarctic Peninsula/Filchner-Ronne Ice Shelf and Ross Ice Shelf regions [Figure 1, *Han et al.*, 2004; *Knudsen*, 2003].

The purpose of this paper is to describe a validation of several published ocean tide models around Antarctica where onshore GPS and gravity data are used to determine site displacements and gravity variations at tidal frequencies respectively, and these are then compared to predictions based on several ocean tide models (via convolution with an Earth model). Such ground-based techniques may be used to assess ocean tide models around Antarctica since the principal contribution to the OTL effect in Antarctica arises from the circum-Antarctic seas [see, e.g., *Agnew*, 1995], although all the world's oceans must be included in the computations.

The only previous studies that have examined OTL gravity variations at Antarctic sites found good agreement between gravity measurements and some models in the longer period tides [*Bos et al.*, 2000; *Sato et al.*, 1997] while larger differences were found in the diurnal and semidiurnal tides [*Agnew*, 1995; *Knopoff et al.*, 1989; *Llubes and Mazzega*, 1997].

However, the only two sites where long records are available (South Pole and Syowa Station – shown in Figure 1 as AMUN and SYOG respectively) are located long distances from the major ice shelves. Consequently, these findings cannot be assumed to be representative of the entire Antarctic continent, especially when considering the energetic diurnal and semidiurnal components. Whilst VLBI measurements have long been shown to also be capable of accurately measuring harmonic ground displacements [*Schuh and Moehlmann*, 1989], the only two VLBI stations in Antarctica (O'Higgins and Syowa, co-located with GPS sites OHIG/OHI2 and SYOG in Figure 1) have insufficient data for the rigorous estimation of OTL displacements (L. Petrov, personal communication, 2003, [*Petrov and Ma*, 2003]). Hence the now relatively dense continuous GPS station coverage across Antarctica (Figure 1), coupled with the millimetric GPS measurement quality of tidal harmonic ground displacement demonstrated by *Allinson et al.* [2004] (that refined the technique first demonstrated by *Schenewerk et al.* [2001]), now makes GPS validation of ocean tide models around Antarctica feasible, with available gravity data providing a supplement.

In Section 2 we overview our selected global and regional ocean tide models and describe the OTL displacement computations. In Section 3 we present our approach for measuring displacements at diurnal and semidiurnal frequencies using GPS and discuss potential systematic errors that may be present in the GPS estimates. In Section 4 we compare each of the GPS and gravity results with modeled estimates and discuss systematic biases in the GPS-derived constituents induced by GPS-dependent errors. The implications of the study are then discussed in Section 5.

2. Ocean Tide Models and Loading Displacements

2.1 Ocean tide modeling background

Whilst the accuracy of ocean tide models improved dramatically during the 1990s to an agreement of 2-3 cm in the deep oceans following the availability (and assimilation) of

TOPEX/Poseidon (T/P) altimetry data [*Andersen et al.*, 1995; *Shum et al.*, 1997], such data only extends to ~66º N/S and hence does not cover most of Antarctica. On a seasonal basis, sea-ice further extends the region where T/P data is unavailable. Unfortunately, tide gauge datasets are also geographically sparse in the circum-Antarctic seas [*Padman et al.*, 2002]. Conventional tidal observations are often not possible although there has been some success in making ice shelf tidal measurements derived using GPS, gravity or remote sensing measurements [*Fricker and Padman*, 2002; *King and Aoki*, 2003], although again these data sets are currently geographically sparse [*Padman et al.*, 2002], limited in accuracy [*Shepherd and Peacock*, 2003] or limited in which tidal constituents may be observed [*Rignot et al.*, 2000].

Compounding the lack of data to assimilate into ocean tide models is the scarcity of bathymetric data which require surface-based seismic surveys in the ice shelf regions, where modeling is further complicated by complex cavity shapes and poorly known frictional regimes. The problems in obtaining bathymetric data are highlighted by the historical problem of defining the location of Antarctica's coastline, since it is typically covered by a continuous sheet of ice. Until the use of remote sensing techniques [*Jezek*, 2002], consistent mapping of the boundary between tidal and non-tidal ice was impossible. An example of this is the Amery Ice Shelf, East Antarctica, where the "grounding zone" was recently redefined to be 230 km further south than previously thought [*Fricker et al.*, 2001]. While this is an extreme example, significant sections of the Antarctic coastline are still not well represented in models and redefinitions of several tens of kilometers are required [*Gray et al.*, 2002]. Since several different versions of coastline definition exist, and it takes time for improvements to be incorporated into model runs, coastline definitions are not consistent between present models.

These uncertainties in the input data have been the reason for excluding the sub ice shelf regions from some models [*Bos et al.*, 2000]. Others have made assumptions about the bathymetric properties of the sub ice shelf cavities in lieu of actual measurements [e.g., *Le Provost et al.*, 1995]. Both scenarios lead to inaccurate modeling of the ocean tides and hence the computed OTL displacement for some Antarctic regions [*Melchior and Francis*, 1996].

2.2 Models selected for validation

Nine published ocean tide models were selected for evaluation, as listed in Table 1. The models consist of gridded amplitudes and phases of the major constituent parts of the total tidal signal, typically including the major semidiurnal M_2, S_2, N_2 and K_2 and diurnal K_1, O_1, P_1 and Q_1 constituents. Seven of the nine models are global models: TPXO.2, TPXO.6, CSR3, FES95.2, FES99, NAO.99b and GOT00.2. Two of the models are non-global models, namely the Circum-Antarctic Tidal Simulation model (CATS02.01) and the Circum-Antarctic Data Assimilation model (CADA00.10), both limited to the oceans south of 58ºS, and for the purpose of OTL computations described below these were supplemented by TPXO.6 north of 60ºS. The uniqueness of each of the models is defined by, for example, the exact model domain (coastline) and bathymetry, the amount and type of data assimilated and the model grid cell interval. Two of the older models (CSR3 and TPXO.2) do not include the regions under the ice shelves and are known to poorly represent these regions as a result [*Melchior and Francis*, 1996]. Several of the newer models have additional data assimilated for the Antarctic region. TPXO.6 uses 324 cycles of T/P data with some small local areas (shallow seas) corrected with higher resolution (0.083º) local inverse solutions, while additional data sets were assimilated for the Ross and Arctic Seas. For the Ross Sea, data from 10 tide gauges was assimilated for the K_1 and O_1 constituents only. In addition, TPXO.6 also incorporates improved bathymetry for the circum-Antarctic seas that has been collated and used in the CATS and CADA models described below (L. Erofeeva, personal

communication, 2003). FES99 has T/P crossover data at 687 deep ocean points and from approximately 700 coastal tide gauges assimilated into a finite element hydrodynamic model. South of 60°S, data were assimilated from approximately eight tide gauges and thirteen T/P crossover points. The P1 constituent is not included in FES99 [*Lefevre et al.*, 2002] and for the loading computations we substituted the values from the TPXO.6 model. The GOT00.2 model used 286 cycles of T/P data to adjust the a priori FES94.1 hydrodynamic model. This model is unique amongst the other models compared here in that 81 cycles of ERS-1 and ERS-2 data are also used at latitudes outside of T/P coverage, although sea ice and ice shelves prevent complete coverage of this region, especially at very high latitudes, meaning that GOT00.2 may resemble FES94.1 around parts of Antarctica. CATS02.01 is a hydrodynamic model driven by TPXO.5.1 sea surface heights along the northern open boundary. CADA00.10 is essentially equivalent to CATS02.01 except that tide gauge, GPS, gravity and T/P data have been assimilated into the model resulting in improved model accuracy, especially in the sub ice shelf regions where data were available [*Padman et al.*, 2002].

While the TPXO.2, CSR3 and NAO.99b models have no data constraining them outside of the T/P boundary they are still of significant value for our comparison since large portions of the East Antarctic and the Antarctic Peninsula coastlines are north of 66ºS or close to this limit (Figure 1). However, we do expect these models to perform more poorly in West Antarctica and in the sub ice shelf areas compared to the other models. As an illustration, Figure 2 shows an example of the level of tidal mismodeling that may occur in sub ice shelf regions by comparing GPS tidal measurements to several ocean tide models for a region near the front of the Amery Ice Shelf [*King*, 2001]. Figure 2 shows that while CADA00.10 and CATS02.01 are in close agreement they have systematically larger amplitude than the GPS (by ~0.05 m). This highlights the fact that agreement between tide

model predictions does not imply tide model accuracy, but possibly only that similar input data have been used in the model runs. The GPS also suggests substantial errors in TPXO.2 and NAO99b, verifying their expected degraded performance at a sub ice shelf location, while this location was outside the CSR3 model domain despite being ~50 km from the nearest coastline. However, independent verification data of the kind shown in Figure 2 are currently sparse and consequently ocean tide models are unverified and poorly constrained by data over large regions of Antarctica. Other methods of model verification are required; onshore OTL displacement or gravity variation measurements are the most convenient examples.

2.3 Modeled ocean tide loading displacements

OTL displacement amplitudes and phase lags were computed using the SPOTL software [*Agnew*, 1997] that uses Green's functions computed by *Farrell* [1972] and the input ocean tide model. OTL displacement estimates were supplied with some of the tide models but for consistency we chose not to use them, instead computing the values using uniform software and procedures. The Antarctic coastline implemented in SPOTL is an updated version of the Antarctic Digital Database version 3 [*ADD Consortium*, 2000]. The updates include the redefinition of the Amery Ice Shelf southern grounding zone and improvements to the Ross Ice Shelf (RIS) eastern grounding zone (D. Agnew, personal communication, 2002). Agreement between different OTL software suites is approximately at the 0.2 mm level [*Scherneck and Bos*, 2002] and hence the choice of software has only a very small contribution to the OTL displacement error budget.

The complex OTL displacement L for a particular location with geographical coordinates (θ', λ') may be computed [*Agnew*, 1997] as:

$$L(\theta',\lambda') = \int_0^{2\pi}\left(\int_0^{\pi}\rho Z(\theta,\lambda)G_L(\Delta)S_L(\alpha)a^2\sin\theta\, d\theta\right)d\lambda \qquad (1)$$

where ρ is the ocean water density, a is the radius of the spherical earth, Z is the complex tidal height at some location (θ,λ), which is a distance Δ at an azimuth α from the point of interest. The function G_L is the mass loading Green's function and S_L is a combination of the trigonometric functions required to compute non-vertical deformations. From the complex tidal height Z the more common tidal amplitude A and phase lags Φ may be computed for comparison with other measurements.

Figure 1 shows the approximate magnitude and spatial variation of total vertical OTL displacements across Antarctica using the CATS02.01 model south of 60°S. (It is noted that GPS does not strictly provide vertical displacement estimates, only radial displacements, but the 'vertical' descriptor will be used throughout the rest of this paper). To account for the far-field OTL we supplemented CATS02.01 with the TPXO.6 model north of 60ºS. Since the ocean tide models are in good agreement in the open ocean, this choice of model is somewhat arbitrary. The OTL displacement estimates shown in Figure 1 were computed on a 2.0º x 0.25º grid at latitudes from 55ºS to 85ºS. Values for latitudes south of 85ºS were computed on a 5.0º x 0.25º grid to reduce computational time, with bicubic interpolation used to form the grid at the full resolution. The notional maximum vertical OTL displacement amplitude at each point on this grid was defined to be:

$$\sigma_{\max} = \sum_{j=1}^{j=8} A_j \qquad (2)$$

where j represents the eight constituents (M_2, S_2, N_2, K_2, O_1, K_1, P_1 and Q_1). The plot of $\sigma_{\max}$ (Figure 1) shows the maximum predicted vertical OTL displacement occurs at a location just to the east of the Antarctic Peninsula where vertical displacements of up to 80 mm (160 mm peak-to-peak) occur. The northern tip of the Antarctic Peninsula undergoes

vertical displacements of up to 70 mm, whilst for the majority of the remainder of the continent the displacement is less than 40 mm, decreasing to 5-10 mm at the South Pole. σ_{max} is, however, an over-estimation since all eight constituents can never be in phase [*Yi et al.*, 2000] and actual maximum displacement amplitudes are approximately 80% of these values.

The accuracy of the modeled OTL displacement will be determined by the input parameters: the ocean tide model errors, the Green's functions and the coastline. Since the latter two are well represented in SPOTL, OTL displacement errors will be dominated by ocean tide model errors. Evaluating Equation 2 for the other models revealed differences between the models near to the Filchner-Ronne and Ross Ice Shelves. For example, inter-model standard deviations at the southern extent of the Filchner-Ronne Ice Shelf approach 10 mm in both M_2 and S_2. These large disagreements are graphically illustrated in Figure 3, with the amplitudes and phase lags shown for a 300° longitudinal profile that crosses the Filchner-Ronne Ice Shelf. A similar pattern is also seen in the other constituents, but with smaller magnitude.

Conversely, the largest variability in the Ross Ice Shelf region is in the O_1 and K_1 constituents, with inter-model standard deviations of 3-4 mm. For the remainder of the Antarctic coastline, the inter-model standard deviation is typically less than 1-2 mm per constituent. This is not surprising, however, as similar input data is present in each of the models in the open ocean (away from the ice shelves or permanent sea ice regions). But, due to reasons mentioned above, this agreement does not necessarily imply accurate modeling of OTL displacements. Therefore, in order to test the accuracy of the OTL displacements (and hence ocean tide models) in the next section we compare modeled OTL displacement estimates against independent harmonic GPS site displacements and gravity variations.

3. GPS Measurements of Ocean Tide Loading Displacements

3.1 Data source

GPS data were collated from 15 permanent receiversites in Antarctica (Figure 1) for the time span 1995.0 to 2003.5. The majority of these sites contribute their data to the International GPS Service (IGS). AMUN and PALM are not part of the IGS network, but data from these sites are also publicly available. Several other groups also kindly provided data from their archives [e.g., *Bouin and Vigny*, 2000]. These continuous sites each had >300 days data (up to ~2700 days), allowing for robust separation of the different major constituents.

3.2 Possible estimation strategies

Several studies have shown that it is possible to measure OTL displacements using geodetic techniques such as GPS [*Allinson et al.*, 2004; *Khan and Tscherning*, 2001] and VLBI [*Petrov and Ma*, 2003; *Schuh and Moehlmann*, 1989]. When compared with VLBI the high spatial density and more complete temporal coverage of continuous GPS sites makes this observing technique particularly attractive. Furthermore, unlike gravity-based techniques, GPS does not suffer from calibration errors nor is it any more problematic in coastal regions than in other locations. Methods previously used for determining the harmonic constituents of surface displacement using GPS fall into two categories. The first involves the determination of sub-daily position estimates (typically 1-4 hr batch sizes) using standard relative GPS positioning techniques where the site motion is regarded as negligible during each batch solution [*Khan and Tscherning*, 2001]. The time series of position estimates may then be treated like independent tide gauge measurements from which the displacement constituents can be computed. The benefit of this method is that it is easy to implement since it requires no changes to conventional GPS processing software. However, for the most precise results an appropriate tropospheric zenith delay estimation frequency must be adopted [*Khan and*

Scherneck, 2003] and the carrier phase ambiguity parameters must be fixed to their correct integer values [*Vey et al.*, 2002]. In fact, if ambiguities are not fixed to integer ambiguities *King et al.* [2003] showed that the horizontal tidal displacement estimates will be biased by up to 40-50% of the magnitude of the vertical signal, although the vertical estimates will still represent the actual vertical motion.

The second method involves treating the harmonic displacement constituents as additional parameters in the GPS processing software [*Allinson et al.*, 2004; *Dach and Dietrich*, 2001; *Schenewerk et al.*, 2001]. This approach allows batch solutions to be computed, thus preserving the long observational arcs that are required for the most accurate geodetic positioning. Given the many thousands of observations present in GPS data spanning 24 hours (the typical static GPS processing window), the additional parameters do not greatly reduce the solution redundancy. Unlike the method above, the parameterization of the harmonic parameters means that ambiguity resolution is not required to determine unbiased horizontal displacement estimates, although this would improve the overall precision of the solution. As a second step, the daily displacement constituent estimates need to be combined using, for example, a Kalman filter.

3.3 Employed estimation strategy

We estimated horizontal and vertical harmonic parameters in a two step process (the second approach outlined above [*Allinson et al.*, 2004]). The first step involved the estimation of the harmonic parameters on a day-by-day basis using the Precise Point Positioning (PPP) technique [*Zumberge et al.*, 1997] in the GIPSY/OASIS-II software [*Webb and Zumberge*, 1995] in 24 h processing sessions. The local east, north and vertical (k = 1,2,3) components of site displacement Δc_k at time t are related to observed OTL displacement amplitudes ($A_{k,j}$) and phase lags ($\Phi_{k,j}$) for component k and constituent j by [*McCarthy*, 1996]

$$\Delta c_k = \sum_{j=1}^{8} f_j A_{k,j} \cos\left(\omega_j t + \chi_j\left(t_0\right) + \mu_j + \Phi_{k,j}\right) \quad (3)$$

To permit linear parameter estimation, Equation 3 may be rewritten in terms of sine and cosine amplitudes as [*Sovers*, 1994]

$$\Delta c_k = \sum_{j=1}^{8}\left[f_j A_{Ck,j} \cos\left(\omega_j t + \chi_j\left(t_0\right) + \mu_j\right) + f_j A_{Sk,j} \sin\left(\omega_j t + \chi_j\left(t_0\right) + \mu_j\right)\right] \quad (4)$$

where f_j and μ_j are needed to account for the modulating effects of the lunar node on the different constituents [*Tamura*, 1987], when only a small subset of constituents are estimated [*McCarthy*, 1996; *Scherneck*, 1999]. χ_j is the astronomical argument at some reference time t_0, chosen here to be J2000, and ω_j is the constituent angular velocity. The magnitudes of the nodal corrections vary over their ~18.6 yr cycle with a maximum amplitude change of approximately ±20% for K_1, K_2, O_1 and Q_1. The other nodal corrections are either small or zero. We adopted the convention of phase lags being negative.

The constituent-related parameters in Equation 4 are A_{Ckj} and A_{Skj}, and one set of these were estimated for each of the eight constituents we considered: M_2, S_2, N_2, K_2, K_1, O_1, P_1 and Q_1 for each of the three coordinate components. In all, 48 additional parameters were estimated compared with a conventional PPP solution. To avoid possible numerical instabilities in the 24 h solutions, we loosely constrained the constituents to their a priori value of 0.0000 m (constraints of 0.20 m and 0.02 m for the vertical and horizontal constituents, respectively). Apart from these additional parameters, we essentially followed the GPS processing strategy described by *Bar-Sever et al.* [1998] using an elevation cut-off angle of 7º, a sampling frequency of 300 s (after data editing and pseudo range smoothing) and estimating tropospheric zenith delays and gradients as random walk parameters at each epoch with process noise values of 10.2 mm/√h and 0.3 mm/√h, respectively [*Lichten*, 1990]. We used the fiducial free orbit and clock products provided by the Jet Propulsion Laboratory (JPL). Ambiguity estimates were not fixed to integer values.

The second step involved the combination of the daily harmonic estimates of A_{Ckj} and A_{Skj} and their variance-covariance matrices in a Kalman filter to produce the final estimates. The Kalman filter was implemented such that its results were equivalent to a weighted mean of the daily constituent estimates. Outliers were rejected using the daily estimates of unit variance. The unit variances were subsequently used in a further iteration of the Kalman filter to re-scale each daily covariance matrix to produce a final unit variance close to 1. Typically, the covariance matrices needed to be scaled by a factor close to 30. For combinations of conventional GIPSY coordinate time series with the same sampling interval and observation weighting scheme this scale factor is typically closer to ~4. The increase is required to account for the increased day-to-day correlations introduced by the simultaneous estimation of harmonic parameters with very similar periods. The mean nodal corrections were then applied to generate the final estimates.

3.4 Sources of bias

For the GPS estimates of harmonic displacement, Δc_j, to accurately represent OTL displacement Δc_{OTL}, other sources of noise or displacement at the tidal frequencies considered must be modeled or eliminated. This may be described as:

$$\Delta c_{OTL,j} = \Delta c_j - \left(\Delta c_{SE,j} + \Delta c_{CM,j} + \Delta c_{Atm,j} + \varepsilon_{GPS} \right) \quad (5)$$

In our analysis, solid earth tides (Δc_{SE}) were corrected (along with pole tides) using the standard models implemented in GIPSY [*McCarthy*, 1996]. The diurnal and semidiurnal solid Earth tides approach zero at high latitudes, and the uncertainties in Earth body tide models are due to anelasticity and are considered to be about 1% of the total Earth body tide at each frequency [*Mathews et al.*, 1997]. Thus at 63°S (the latitude where this error will be

greatest in our network), the contribution to Equation 5 from solid Earth tide mismodeling can be considered ~0.7 mm (K_1) and ~0.5 mm (O_1) in the vertical component, with the other constituents having uncertainties <0.3 mm. These uncertainties reduce to zero at AMUN since the solid earth tide at these frequencies is theoretically zero there. Consequently, any mismodeling may be evident in our data set, especially for O_1 which has the largest amplitude of those constituents free from other known systematic biases. At similar latitudes, any mismodeling will exhibit itself as a constant bias and hence should be evident in our estimates, depending on solution precision. Sub-daily geocenter motions at tidal frequencies (Δc_{CM}) are neglected at the stage of fiducial-free orbit computation at JPL but previous studies have shown that PPP solutions using the JPL products are insensitive to these geocenter motions [*Scherneck et al.*, 2000]. Furthermore, diurnal and semidiurnal radiational atmospheric tides (Δc_{Atm}) are negligible at high latitudes [*Ray and Ponte*, 2003].

Other than these genuine sources of displacement, other apparent signals may also bias the estimation process, most notably from unmodeled systematic errors in the GPS observations themselves (ε_{GPS}). For example, the orbital period of the GPS satellites is close to one-half a sidereal day (K_2) and the constellation repeat period is close to one sidereal day (K_1), and these have been suggested as a reason for constituent bias in previous studies [*Schenewerk et al.*, 2001] via GPS satellite orbit mismodeling and/or multipath. Since there is not yet a well-established method for modeling multipath and orbit modeling requires further theoretical development, we expected some GPS-based biases to be evident in the displacement constituent estimates. Second order ionospheric effects [*Kedar et al.*, 2003] will also be present (close to S_1) but since we do not solve for a parameter at this frequency the daily diurnal constituent estimates will likely be adversely affected, most notably the solar-related K_1 and P_1. It is conceivable that second order ionospheric effects may also bias S_2, but their magnitude at this frequency is presently unclear. Importantly, apart from multipath and

other site specific errors, these potential sources of OTL displacement bias should express themselves in terms of misfits that are regionally correlated.

3.5 Constituent convergence

Due to the high between-constituent correlation introduced by our estimation strategy and according to the Rayleigh criterion [e.g., *Pugh*, 1987], the constituent estimates vary considerably during the first few hundred days. *Allinson et al.* [2004] showed that, on average, GPS estimates of the most energetic constituents (such as M_2) will be in agreement (at the 1 mm level) with long-term values by combining approximately 90 days of data. However, since we are aiming to determine reliable estimates of all eight major constituents (including those with sub-mm magnitudes) this value may be regarded as an absolute minimum data span. To assess when a particular constituent had stabilized sufficiently within the Kalman filter, we determined the data count after which additional data does not significantly affect the result (here chosen so that if the parameter estimates were in agreement to within 0.5 mm and 5° for 300 consecutive solution updates the solution was deemed to have stabilized. The stabilization point for each constituent was then the beginning of this window of 300 consecutive solutions). The stabilization time plotted against the estimated constituent amplitude is shown in Figure 4 using data from all sites. The number of daily solutions required for the constituents to stabilize appears to be an approximately exponential function of constituent amplitude for each of the coordinate components, from the lower limit of approximately 280 days. There is, however, some variation in the amount of data required prior to stabilization for any amplitude. For example, a 10 mm vertical signal may take between 350 and 1200 days to stabilize, while the different constituents are generally uniformly distributed.

4. Comparison of GPS and gravity estimates with modeled and other GPS values

4.1 GPS Results

The three-dimensional harmonic displacement estimates computed as described above are listed in Table 2, and according to Equation 5 we interpret these as being dominated by OTL displacements with the possible exception of K_1 and K_2. The constituent estimates did not stabilize at three sites (CONZ, ELHT and ROTH) and hence these estimates should be regarded with caution. Indeed, CONZ and ELHT are only 3 km apart and within a few tens of kilometers from MCM4, but their constituent estimates are quite different, especially for K_1 and K_2. Their formal errors are significantly greater (about twice) those of OHI2 which has a similar number of data days, suggesting that the data noise is high at CONZ and ELHT. It should also be noted that both CONZ and ELHT are located on an active volcano and its own motion at these frequencies is unknown. Conversely, the estimates at OHIG and OHI2, separated by a few hundred metres and using data collected at completely different times, are in agreement within their one sigma noise levels (apart from K_2) following constituent convergence.

Figures 5-7 show phasor plots of GPS and model estimates for the east, north and vertical components respectively for DUM1 which is in a region (East Antarctica, Figure 1) where the tidal signal is well known and hence the ocean tide models are in good agreement. The GPS estimates of the horizontal displacements are each in agreement with the models within their 95% confidence limits (apart from the disagreement with K_1 and K_2 which is discussed in more detail below). In fact, the agreement between the model and GPS estimates of Q_1 and N_2 are at the sub-millimeter level for each of the three coordinate components.

To assess the level of agreement between the GPS estimates and the models at each site we computed a misfit test statistic (S^2) defined as the sum of the squares of the complex differences

$$S^2 = \sum_{k=1}^{3} \sum_{j=1}^{8} \left(\left| Z_{GPS_{j,k}} - Z_{Model_{j,k}} \right|^2 \right) \quad (6)$$

Likewise, the uncertainties of the GPS estimates are propagated into estimates of σ_{S^2}, although, as is common in tidal gravity studies, the model estimates were assumed to be error free, since formal errors are not typically available for ocean tide models.

Figure 8 shows S^2 for each of the models tested at twelve sites, for both the vertical-only misfit (light grey bars) and the total three-dimensional misfit (dark grey bars). The left hand bars for each model represent the misfit for all eight constituents, whilst the right hand bars exclude K_1 and K_2 due to their consistently higher levels of misfit when compared with the other constituents. For example, there are very large horizontal misfits at VESL where the GPS estimates show ~5 mm east and north signals for K_2 (Table 2) whilst the model values do not exceed ~0.5 mm. K_1 is also biased by several millimeters. A large reduction in the horizontal misfit is evident following the removal of K_1 and K_2 from the computation (Figure 8, right hand bars). Similar, although smaller, improvements are obtained at the other sites with large horizontal misfits (AMUN, OHIG, ROTH and SYOG) when K_1 and K_2 are omitted. In addition, large reductions in the vertical misfits are also evident at all sites when K_1 and K_2 are removed.

The poor GPS-model agreements at the K_1 and K_2 frequencies are further illustrated in Figure 9. This shows a box-and-whisker plot of the residuals (magnitudes of the vector difference between the GPS and TPXO.6 modeled estimates) for each constituent, according to coordinate component for all 15 sites. Compared with the other constituents K_2, and to a slightly lesser extent K_1, have larger residuals for each of the coordinate components. Figure 9 also reveals that the N_2 and Q_1 residuals are particularly small across all three coordinate components, averaging 0.27 mm and 0.44 mm respectively for the vertical residual and ~0.15 mm for the horizontal residuals for both constituents. There is no consistent difference

between the residuals of the solar-related constituents compared to the lunar-only constituents suggesting that solar-related GPS errors (e.g., GPS orbit mis-modeling) are not dominant. There is no clear latitude-dependent pattern in the O_1 residuals that would point towards the detection of solid earth tide deformation modeling errors, while K_1 estimates are not sufficiently reliable to be useful in this regard. Importantly, the level of misfit for N_2 and Q_1 is beginning to approach the level of agreement between the different OTL software [*Scherneck and Bos*, 2002].

The absorption of systematic errors into K_2 is somewhat difficult to explain as the GPS constellation repeats at the K_1 period and hence a K_2 bias suggests satellite-dependent errors (since the satellite orbit and K_2 periods are equal). Satellite-dependent errors would be expected to bias sites within the same region to a similar extent. Figure 10 shows the amplitudes and phase lags of the K_1 and K_2 residuals after subtracting the TPXO.6 value for each of the north, east and vertical components. The K_2 residuals demonstrate a consistent ~90° phase difference between the east and north residuals, with near identical magnitude. This suggests satellite-dependent biases which result in an apparent circular horizontal motion of the antenna. The vertical residuals also show a similar magnitude to the horizontal misfits. Since the GPS estimates for the various sites have been generated using different observation periods, Figure 10 was reproduced using the data for the same period (2002.0-2003.5) for sites where complete data coverage existed. However, no changes to the patterns shown in Figure 10 were evident. We suggest that one possible mechanism for the K_2 bias is satellite-dependent range biases interacting with local obstructions to produce the evident site-dependency.

The K_1 bias shows a different pattern, with a greater randomness in the relative phases of the east, north and vertical component misfits. No regional correlation is evident either, at least at the few-hundred-kilometer level and greater. For example, the sites along the

Antarctic Peninsula have very different K_1 misfits in terms of amplitude and phase. Since a similar pattern to K_2 would be expected if orbit related effects were dominant, we suggest that the majority of the K_1 bias has its source in site-dependent effects such as multipath. Due to the (likely GPS incurred) systematic biases present on K_1 and K_2, for the assessment of the ocean tide models only the remaining six constituents are considered (the right hand bars in Figure 8).

In East Antarctica, misfits are uniform across all models for the sites DUM1, CAS1, DAV1 and MAW1 due to the sub-mm agreement between the models in this region. SYOG is the only exception where the CSR3 and GOT00.2 models have larger misfits. The three-dimensional misfit values are as low as 3.6 mm^2 (DAV1), with the vertical-only misfits as low as 1.2 mm^2. The lowest vertical misfits are not significantly different from zero at the two sigma level for any of these sites. As expected, the inter-model variability at sites in West Antarctica is greater, although several models at each site produce, within their confidence levels, similarly low misfits to the East Antarctic sites (Figure 8).

Notably, the models that agree best with the GPS estimates are those that have had particular focus on these regions in order to improve the modeling there. Table 3 lists the smallest misfit with the corresponding model, for both the three-dimensional and vertical-only cases. After ranking the three-dimensional model misfits for each site (not shown), TPXO.6, FES99 and CADA00.10 consistently appear in the first few places. When only the vertical component is considered, TPXO.6, CADA00.10, FES99 and CATS02.01 consistently rank highest. The misfit significances computed according to the Student's t-test are shown in Figure 11. Closer agreement (i.e., smaller misfit) between GPS and model estimates is reflected by lighter shades of grey in Figure 11 and vice versa. For most sites the three-dimensional misfits (Figure 11a) are highly significant, with only the sites with shorter time series (and hence higher formal errors) having low significance. The vertical-only

significances (Figure 11b) are more informative in terms of separating the various models. Misfits for TPXO.6 are consistently of equal or lower significance than for the other models (apart from OHIG). Near the Filchner-Ronne Ice Shelf (OHIG, OHI2, PALM, ROTH, BELG), misfits with FES99 have the lowest significance. For the sites near large ice shelves (MCM4, ROTH, BELG, PALM, OHI2 and OHIG) TPXO.2, CSR3 and NAO.99b provide significantly worse fits. As with the three-dimensional misfits, all misfits are highly significant at SYOG. Examining the differences on a constituent-by-constituent basis shows that this is caused by disagreements on several constituents (all but N_2) and we suspect that the GPS estimates are erroneous at this site.

Given the care taken with data assimilation and the construction of bathymetric data sets for this region, the geographically widespread accuracy of CADA00.10, CATS02.01 and TPXO.6 across Antarctica is not surprising. As mentioned above, the large misfits with CSR3 and TPXO.2 (on average 330% and 442% larger than the TPXO.6 misfits, respectively, in West Antarctica) is not unexpected and these models should not be used near the large ice shelves. The large misfit with NAO.99b (on average 400% larger than the TPXO.6 misfits in West Antarctica) is somewhat unexpected since it agrees at the 0.02 m level (comparing ocean tide height on a per-constituent basis) with other modern models in a global sense [*Matsumoto et al.*, 2000]. However, with the absence of data outside of the T/P observation region only the hydrodynamic equations constrain the model around Antarctica.

4.2 Comparison with Schenewerk et al. GPS estimates

For some of the sites in the present study GPS estimates of OTL displacement (vertical only) have been previously published by *Schenewerk et al.* [2001]. The results from their study, referred to hereafter as 'NGS' (i.e., National Geodetic Survey), are available at http://www.ngs.noaa.gov/GRD/GPS/Projects/OLT/Ets.00aug31/ets.html, although the web results are more recent than those described in *Schenewerk et al.* [2001], using a longer data

time series (1994-1999 inclusive, M. Schenewerk, personal communication, 2004). The NGS estimates were produced as part of their routine global analyses, which also includes the estimation of satellite orbits and Earth orientation parameters. Six years of data were processed, similar to the data span in our solutions. While only every third day (a maximum of ~1100 days) was used in the final solution, combining the entire data set did not produce significantly different results [*ibid.*]. Misfits between our vertical estimates and the NGS estimates were computed and are shown in Figure 8 alongside the misfits with the modeled OTL displacements discussed previously. In each case, the NGS misfits are much larger than 100 mm^2 – in fact, the NGS constituents are consistently 20-60% larger in amplitude than our estimates and there are also large differences in phase. These misfits are much larger than the combined uncertainties of the two sets of estimates. Interestingly, the NGS estimates have much smaller formal errors than ours despite using much less data. For example, at MAW1 the NGS M_2 amplitude estimate has uncertainties of ~0.2 mm per complex component, whilst our own estimates, using every third day over a six year period (1995.0-2001.0), yielded formal errors of ~1.7 mm per complex component, almost an order of magnitude larger (using the full dataset the formal errors are ~0.8 mm). However, even after applying these revised uncertainty estimates to the NGS results they are different from our own results at the 95% confidence level. A comparison between the NGS and the ocean tide model estimates also shows a much larger misfit than is evident between our own estimates and the models. Consequently, we conclude that the majority of these misfits have their origin in the NGS results.

4.3 Gravity Results

Independent ocean tide model verification information may also be obtained from long-term gravity data, such as the time series collected at the South Pole (AMUN). Following a tidal analysis on these gravity data, constituent amplitudes and phase lags were

tabulated by *Knopoff et al.* [1989]. The gravity tidal record is clearly superior to the GPS record since the GPS formal errors at AMUN are comparable to the measured signal there while the uncertainty in each of the gravity-derived constituents is negligible [*Agnew*, 1995]. The location of AMUN is important since the closest seas are those under the Ross and Filchner-Ronne ice shelves where GPS data is lacking. Previous studies have compared the gravity record at AMUN with model estimates and found increasing improvement as newer models were developed [*Agnew*, 1995; *Llubes and Mazzega*, 1997]. Table 4 shows the vector differences between gravity and the models and each of the major constituents as well as S^2, while Figure 12 shows a subset of the model estimates in terms of a phasor plot. Of the model estimates listed, only FES95.2 has been previously shown in comparison to AMUN [*Agnew*, 1995], with the largest reported misfits being for O_1 and S_2.

Figure 12 shows that the newer models represent a further improvement on the agreement demonstrated using FES95.2 (shown as a filled triangle). Most notable are the reduced misfits of S_2 and K_1. However, the majority of models fail to reproduce the M_2 signal with the same accuracy as S_2 and K_1; only FES99 accurately represents it. The scatter of the modeled O_1 estimates remains the highest, with TPXO.6, CATS02.01 and CADA00.10 best representing the gravity measurement. As indicated in the GPS data, NAO.99b is clearly erroneous for almost all of the constituents (Table 4), while overall TPXO.6, CADA00.10, FES99 and CATS02.01 fit the gravity measurements better than the previous best model (FES95.2). Indicatively, these are the same four models in the same order as those that best fit the GPS vertical displacement estimates when considering all fifteen GPS sites.

5. Discussion and Conclusions

This study has demonstrated that a number of recent ocean tide models accurately predict OTL displacements around Antarctica as determined by GPS at 15 sites and by relative gravity at the South Pole. In terms of ocean tide model recommendations for

Antarctica, *Agnew* [1995], *Llubes and Mazzega* [1997] and *Melchior and Francis* [1996] concluded that the only appropriate tide models were the FES series of models (up to the FES95.2 model available at that time). We suggest a replacement list comprising the global TPXO.6 and FES99 models and the regional Antarctic CATS02.01 and CADA00.01 models, whereas CSR3, TPXO.2 and NAO.99b are only suitable away from the large ice shelves. The poor performance of NAO.99b will explain the majority of the apparently large aliased signal shown in this region in *Han et al.* [2004]. Figure 3 also reveals that S_2 is erroneously determined in FES95.2 under the Filchner-Ronne Ice Shelf (as reported for other regions) and may partially explain the GPS misfit with this model reported in *Dach and Dietrich* [2001].

Around East Antarctica, there is little difference between the various models of OTL displacement, although the differences have not been evaluated at the southern extent of the Amery Ice Shelf where ocean tide models are divergent. The greatest variations in modeled OTL displacement are around the Filchner-Ronne Ice Shelf, and it is at the GPS sites in this region that the accuracy of FES99, TPXO.6 and CADA00.10 is most evident. While we have not included the CSR4 model in the comparisons shown here, it is little changed from CSR3 around Antarctica and hence its use is also likely not suitable near the large ice shelves.

The ocean tide model recommendation are of particular importance to GRACE gravity field reductions, altimeter ice elevation studies, InSAR ice shelf velocity determination and onshore GPS measurements, amongst others. For example, measurements of Antarctic ice surface elevations using the Geoscience Laser Altimeter System (GLAS) onboard ICESat [*Zwally et al.*, 2002], CryoSat or airborne systems [*Thomas et al.*, 2004] will be affected by OTL displacement [*Yi et al.*, 2000] and displacements computed using the GOT00.2 model are being distributed with GLAS products. Figure 3 shows that M_2 and S_2 amplitude differences between FES99 and GOT00.2 are 3-5 mm and 2-3 mm respectively in the Filchner-Ronne Ice Shelf region. To assess the level of possible bias on GLAS

measurements we computed OTL displacements for the southern Filchner-Ronne region (Figure 13) using both FES99 and GOT00.2. We computed the displacements for locations along the ground-track of the 33-day near-sub-cycle of the 91-day ICESat orbit; the laser was regarded as being switched off for the remainder of the 91-day orbit. An along-track sampling interval of 1 sample per 2 seconds (approximately 16 km) was used. Since the displacement depends on the time of over-flight we sampled a series of 2 year periods of model differences with a nominal start day of Jan 1, 2002. This start time was stepped by 1 hr increments until the full semidiurnal/diurnal cycle was sampled. For each increment we computed elevation rates at each measurement location due only to the difference between FES99 and GOT00.2. The absolute maximum and RMS of this time series were then computed and are shown in Figure 13a and b respectively. Over Berkner Island and nearby islands the choice of ocean tide model will alter the estimated rates by up to ±2.0-2.5 mm/yr. The uncertainty decreases rapidly to zero southward of the coastline where the models converge (Figure 3). However, the potential error is larger when fewer measurements epochs are available, such as is common in airborne altimeter studies [e.g., *Thomas et al.*, 2004].

In regions where the ocean tides are well known, agreements between the GPS and model displacement values are sub-mm in all three-dimensions. Independent estimates at the same location (OHIG/OHI2) using different data sets show agreements within the formal errors. The number of sites where reliable estimates are possible will continue to expand and random errors continue to reduce as the data archive increases with time. Further addressing systematic errors in the GPS measurements will enable all eight major diurnal/semidiurnal constituents to be determined at the level of accuracy demonstrated for N_2 and Q_1. While we have demonstrated this potential for the Antarctic region, such accuracies should also be achievable at hundreds of global permanent GPS sites where continuous data records are often approaching one decade and where many are at latitudes where the satellite

constellation is more evenly distributed across the sky than in Antarctica. Despite this approach requiring long data records and being presently affected by systematic errors, GPS has some advantages over gravimetric methods for OTL measurements, including the lack of sensitivity to small changes in mass and no requirement for regular calibration (K_1 and K_2 aside). Currently, permanent VLBI and superconducting gravimeter sites number ~50 and 20 respectively, many of which have co-located GPS measurements. Inter-comparison of estimates at these sites will demonstrate the lower limit of accuracy of GPS-based measurements.

While GPS-based estimates are currently limited in some constituents due to the orbital period of the GPS satellites, other global satellite navigation systems are not; both the GLONASS (~11.25 hr) and the forthcoming Galileo (proposed ~14.37 hr) constellations have orbital periods at non-tidal frequencies. A combined solution, using appropriate constituent-dependent weighting, may allow for the unbiased estimation of these currently problematic constituents. If successful, such a combination promises sub-mm constituent accuracies at all eight of the major semidiurnal and diurnal tidal frequencies.

While we have considered the signals affecting the sidereal and half-sidereal constituents as biases here, there are evidently unmodeled GPS systematic errors which may be approximated by these purely harmonic parameters. Consequently, while these signals are non-tidal in origin they may still propagate into GPS coordinate time series at semi-annual and annual periods [*Penna and Stewart*, 2003]. Their amplitude routinely exceeds 2 mm at the sites considered here. Rather than implementing standard ocean tide models to compute modeled displacements at these sites, greater time series precision may therefore be obtained by implementing the "biased" estimates determined by GPS, or estimating harmonic parameters on a day-by-day basis to account for the sub-daily systematic errors. Better

understanding of these systematic errors will not only aid tidal estimation but also long-term velocity and global loading estimates and GPS-derived precipitable water vapor estimates.

In terms of further progression of the ocean tide models around Antarctica, the quality of the bathymetric information and the degree of data assimilation remain the limiting factors. It is difficult to envisage significant improvements beyond the performance of the best models without greater spatial density of water column thickness information in the sub ice shelf regions and/or without tidal data being assimilated at more points. Even the best models in our revised list produce OTL displacement estimates with differences of several millimeters at the southern extents of the large ice shelves. Further in situ data is required to reduce these uncertainties to negligible levels.

Acknowledgements

This project was enabled by the free provision of data from many sources. Ocean tide model outputs were made freely available by the authors and GPS data were made available through the public archives of the IGS, CDDISA, UNAVCO and SCAR, and additional data from Atsushi Yamagiwa, Hans-Werner Schenke, Daniel Schulte, Paul Tregoning, Andrea Donnellan, Marie-Noelle Bouin and Gordon Hamilton. We thank JPL for providing their GIPSY/OASIS II software and orbit products and Frank Wu for providing modified routines. Duncan Agnew kindly supplied his SPOTL software. This paper was substantially improved following the careful reviews of three anonymous reviewers and comments from the Associate Editor. Some of the figures were generated using the Generic Mapping Tools (GMT) [*Wessel and Smith*, 1998].

References:

ADD Consortium, Antarctic Digital Database, Version 3.0. Database, manual and bibliography, pp. 93, Scientific Committee on Antarctic Research., Cambridge, 2000.

Agnew, D.C., Ocean-load tides at the South Pole - a validation of recent ocean-tide models, *Geophysical Research Letters*, *22* (22), 3063-3066, 1995.

Agnew, D.C., NLOADF: A program for computing ocean-tide loading, *Journal of Geophysical Research*, *102* (B3), 5109-5110, 1997.

Allinson, C.R., P.J. Clarke, S.J. Edwards, M.A. King, T.F. Baker, and P.R. Cruddace, Stability of direct GPS estimates of ocean tide loading, *Geophysical Research Letters*, *31*, L15603, doi:10.1029/2004GL020588, 2004.

Anandakrishnan, S., D.E. Voigt, R.B. Alley, and M.A. King, Ice stream D flow speed is strongly modulated by the tide beneath the Ross Ice Shelf, *Geophysical Research Letters*, *30* (7), 1361, doi:10.1029/2002GL016329, 2003.

Andersen, O.B., P.L. Woodworth, and R.A. Flather, Intercomparison of recent ocean tide models, *Journal of Geophysical Research*, *100* (C12), 25261-25282, 1995.

Bar-Sever, Y.E., P.M. Kroger, and J.A. Borjesson, Estimating horizontal gradients of tropospheric path delay with a single GPS receiver, *Journal of Geophysical Research*, *103* (B3), 5019-5035, 1998.

Bos, M.S., T.F. Baker, F.H. Lyard, W.E. Zürn, and P.A. Rydelek, Long-period lunar Earth tides at the geographic South Pole and recent models of ocean tides, *Geophysical Journal International*, *143*, 490-494, 2000.

Bouin, M.N., and C. Vigny, New constraints on Antarctic plate motion and deformation from GPS data, *Journal of Geophysical Research*, *105* (B12), 28279-28293, 2000.

Dach, R., and R. Dietrich, The ocean loading effect in GPS analysis: A case study in the Antarctic Peninsula region, *Marine Geodesy*, *24*, 13-25, 2001.

Dietrich, R., R. Dach, G. Engelhardt, J. Ihde, W. Korth, H. Kutterer, K. Lindner, M. Mayer, F. Menge, H. Miller, C. Muller, W. Niemeier, J. Perlt, M. Pohl, H. Salbach, H.W. Schenke, T. Schone, G. Seeber, A. Veit, and C. Volksen, ITRF coordinates and plate velocities from repeated GPS campaigns in Antarctica - an analysis based on different individual solutions, *Journal of Geodesy*, *74*, 756-766, 2001.

Eanes, R.J., Diurnal and semidiurnal tides from TOPEX/POSEIDON altimetry, *Eos Trans. AGU*, *75* (16), 108, 1994.

Egbert, G.D., A.F. Bennett, and M.G.G. Foreman, TOPEX/POSEIDON tides estimated using a global inverse model, *Journal of Geophysical Research*, *99* (C12), 24821-24852, 1994.

Farrell, W.E., Deformation of the earth by surface loads, *Reviews of Geophysics and Space Physics*, *10* (3), 761-797, 1972.

Fricker, H.A., I. Allison, M. Craven, G. Hyland, A. Ruddell, N. Young, R. Coleman, M. King, K. Krebs, and S. Popov, Redefinition of the Amery Ice Shelf, East Antarctica, grounding zone, *Journal of Geophysical Research*, *107* (5), doi: 10.1029/2001JB000383, 2001.

Fricker, H.A., and L. Padman, Tides on Filchner-Ronne Ice Shelf from ERS radar altimetry, *Geophysical Research Letters*, *29* (12), 1622, doi:10.1029/2001GL014175, 2002.

Gray, L., N. Short, R. Bindschadler, I. Joughin, L. Padman, P. Vornberger, and A. Khananian, RADARSAT interferometry for Antarctic grounding-zone mapping, *Annals of Glaciology*, *34*, 269-276, 2002.

Han, S.C., C. Jekeli, and C.K. Shum, Time-variable aliasing effects of ocean tides, atmosphere, and continental water mass on monthly mean GRACE gravity field, *Journal of Geophysical Research*, *109* (B4), doi: 2003JB002501/B04403, 2004.

Jezek, K.C., RADARSAT-1 Antarctic Mapping Project: change-detection and surface velocity campaign, *Annals of Glaciology*, *34*, 263-268, 2002.

Kedar, S., G.A. Hajj, B.D. Wilson, and M.B. Heflin, The effect of the second order GPS ionospheric correction on receiver positions, *Geophysical Research Letters*, *30* (16), 1829, doi:10.1029/2003GL017639, 2003.

Khan, S.A., and H.G. Scherneck, The M_2 ocean tide loading wave in Alaska: vertical and horizontal displacements, modelled and observed, *Journal of Geodesy*, *77* (3-4), 117-127, doi: 10.1007/s00190-003-0312-y, 2003.

Khan, S.A., and C.C. Tscherning, Determination of semi-diurnal ocean tide loading constituents using GPS in Alaska, *Geophysical Research Letters*, *28* (11), 2249-2252, 2001.

King, M., The dynamics of the Amery Ice Shelf from a combination of terrestrial and space geodetic data, Unpublished PhD thesis, University of Tasmania, Hobart, 2001.

King, M., and S. Aoki, Tidal observations on floating ice using a single GPS receiver, *Geophysical Research Letters*, *30* (3), 1138, doi:10.1029/2002GL016182, 2003.

King, M., R. Coleman, and L. Nguyen, Spurious periodic horizontal signals in sub-daily GPS position estimates, *Journal of Geodesy*, *77* (1-2), 15-21, doi:10.1007/s00190-002-0308-z, 2003.

King, R.W., and Y. Bock, Documentation for the GAMIT GPS analysis software (version 10.0), Unpublished, Massachusetts Institute of Technology, Cambridge, 2001.

Knopoff, L., P.A. Rydelek, W. Zurn, and D.C. Agnew, Observations of load tides at the South-Pole, *Physics of the Earth and Planetary Interiors*, *54* (1-2), 33-37, 1989.

Knudsen, P., Ocean tides in GRACE monthly averaged gravity fields, *Space Science Reviews*, *108* (1-2), 261-270, 2003.

Le Provost, C., M.L. Genco, and F. Lyard, Modeling and predicting tides over the World Ocean, in *Quantitative Skill Assessment for Coastal Ocean Models*, pp. 175-201, American Geophysical Union, 1995.

Le Provost, C., F. Lyard, J.M. Molines, M.L. Genco, and F. Rabilloud, A hydrodynamic ocean tide model improved by assimilating a satellite altimeter-derived data set, *Journal of Geophysical Research*, *103* (C3), 5513-5529, 1998.

Lefevre, F., F.H. Lyard, C. Le Provost, and E.J.O. Schrama, FES99: A global tide finite element solution assimilating tide gauge and altimetric information, *Journal of Atmospheric and Oceanic Technology*, *19* (9), 1345-1356, 2002.

Lichten, S.M., Estimation and filtering for high-precision GPS positioning applications, *Manuscripta Geodaetica*, *15*, 159-176, 1990.

Llubes, M., and P. Mazzega, Testing recent global ocean tide models with loading gravimetric data, *Progress in Oceanography*, *40* (1-4), 369-383, 1997.

Manson, R., R. Coleman, P. Morgan, and M. King, Ice velocities of the Lambert Glacier from static GPS observations, *Earth Planets and Space*, *52* (11), 1031-1036, 2000.

Mathews, P.M., V. Dehant, and J.M. Gipson, Tidal station displacements, *Journal of Geophysical Research*, *102* (B9), 20469-20477, 1997.

Matsumoto, K., T. Takanezawa, and M. Ooe, Ocean tide models developed by assimilating TOPEX/POSEIDON altimeter data into hydrodynamical model: A global model and a regional model around Japan, *Journal of Oceanography*, *56* (5), 567-581, 2000.

McCarthy, D.D., IERS Conventions (1996), IERS Technical Note 21, pp. 95, International Earth Rotation Service, 1996.

Melchior, P., and O. Francis, Comparison of recent ocean tide models using ground-based tidal gravity measurements, *Marine Geodesy*, *19*, 291-330, 1996.

Padman, L., H.A. Fricker, R. Coleman, S. Howard, and L. Erofeeva, A new tide model for the Antarctic ice shelves and seas, *Annals of Glaciology*, *34*, 247-254, 2002.

Penna, N.T., and M.P. Stewart, Aliased tidal signatures in continuous GPS height time series, *Geophysical Research Letters*, *30* (23), 2184, doi:10.1029/2003GL018828, 2003.

Petrov, L., and C.P. Ma, Study of harmonic site position variations determined by very long baseline interferometry, *Journal of Geophysical Research*, *108* (B4), 2190, doi:10.1029/2002JB001801, 2003.

Pugh, D.T., *Tides, surges and mean sea-level: a handbook for engineers and scientists*, 472 pp., John Wiley and Sons, Chichester, 1987.

Ray, R.D., A global ocean tide model from TOPEX/POSEIDON altimetry: GOT99.2, NASA Technical Memorandum 209478, pp. 58, 1999.

Ray, R.D., and R.M. Ponte, Barometric tides from ECMWF operational analyses, *Annales Geophysicae*, *21*, 1897-1910, 2003.

Rignot, E., L. Padman, D.R. MacAyeal, and M. Schmeltz, Observation of ocean tides below the Filchner and Ronne Ice Shelves, Antarctica, using synthetic aperture radar interferometry: Comparison with tide model predictions, *Journal of Geophysical Research*, *105* (C8), 19615-19630, 2000.

Sato, T., M. Ooe, K. Nawa, K. Shibuya, Y. Tamura, and K. Kaminuma, Long-period tides observed with a superconducting gravimeter at Syowa station, Antarctica, and their implication to global ocean tide modeling, *Physics of the Earth and Planetary Interiors*, *103* (1-2), 39-53, 1997.

Schenewerk, M.S., J. Marshall, and W. Dillinger, Vertical ocean-loading deformations derived from a global GPS network, *Journal of the Geodetic Society of Japan*, *47* (1), 237-242, 2001.

Scherneck, H.-G., Explanatory supplement to the section "Local site displacement due to ocean loading" of the IERS Conventions (1996), in *Explanatory supplement to the IERS Conventions (1996) Chapters 6 and 7*, edited by H. Schuh, pp. 29, Deutsches Geodätisches Forschungsinstitut, Munich, 1999.

Scherneck, H.-G., and M.S. Bos, Ocean tide and atmospheric loading, in *International VLBI Service for Geodesy and Astronomy 2002 General Meeting*, edited by N.R. Vandenberg, and K.D. Baver, NASA/CP-2002-210002, Tsukuba, 2002.

Scherneck, H.-G., J.M. Johansson, and F.H. Webb, Ocean loading tides in GPS and rapid variations of the frame origin, in *Geodesy beyond 2000—The Challenges of the First Decade, IAG General Assembly*, edited by K.-P. Schwarz, pp. 32-40, Birmingham, 2000.

Schuh, H., and L. Moehlmann, Ocean loading station displacements observed by VLBI, *Geophysical Research Letters*, *16* (10), 1105-1108, 1989.

Shepherd, A., and N.R. Peacock, Ice shelf tidal motion derived from ERS altimetry, *Journal of Geophysical Research*, *108* (C6), art. no.-3198, 2003.

Shum, C.K., P.L. Woodworth, O.B. Andersen, G.D. Egbert, O. Francis, C. King, S.M. Klosko, C. Le Provost, X. Li, J.M. Molines, M.E. Parke, R.D. Ray, M.G. Schlax, D. Stammer, C.C. Tierney, P. Vincent, and C.I. Wunsch, Accuracy assessment of recent ocean tide models, *Journal of Geophysical Research*, *102* (C11), 25173-25194, 1997.

Sovers, O.J., Vertical ocean loading amplitudes from VLBI measurements, *Geophysical Research Letters*, *21* (5), 357-360, 1994.

Tamura, Y., A harmonic development of the tide-generating potential, *Bulletin D'Informations Marees Terrestres*, *99*, 6813-6857, 1987.

Tapley, B.D., S. Bettadpur, J.C. Ries, P.F. Thompson, and M.M. Watkins, GRACE measurements of mass variability in the Earth system, *Science*, *305* (5683), 503-505, 2004.

Thomas, R., E. Rignot, G. Casassa, P. Kanagaratnam, C. Acuna, T. Akins, H. Brecher, E. Frederick, P. Gogineni, W. Krabill, S. Manizade, H. Ramamoorthy, A. Rivera, R. Russell, J. Sonntag, R. Swift, J. Yungel, and J. Zwally, Accelerated sea-level rise from West Antarctica, *Science*, *306* (5694), 255-258, 2004.

Tregoning, P., A. Welsh, H. McQueen, and K. Lambeck, The search for postglacial rebound near the Lambert Glacier, Antarctica, *Earth Planets and Space*, *52* (11), 1037-1041, 2000.

Vey, S., E. Calais, M. Llubes, N. Florsch, G. Woppelmann, J. Hinderer, M. Amalvict, M.F. Lalancette, B. Simon, F. Duquenne, and J.S. Haase, GPS measurements of ocean loading and its impact on zenith tropospheric delay estimates: a case study in Brittany, France, *Journal of Geodesy*, *76* (8), 419-427, 2002.

Webb, F.H., and J.F. Zumberge, An introduction to GIPSY/OASIS-II precision software for the analysis of data from the Global Positioning SystemJPL D-11088, Jet Propulsion Laboratory, Pasadena, CA, 1995.

Wessel, P., and W.H.F. Smith, New, improved version of Generic Mapping Tools released, *EOS Transactions of the American Geophysical Union*, *79* (47), 579, 1998.

Yi, D., J.B. Minster, and C.R. Bentley, The effect of ocean tidal loading on satellite altimetry over Antarctica, *Antarctic Science*, *12* (1), 119-124, 2000.

Zumberge, J.F., M.B. Heflin, D.C. Jefferson, M.M. Watkins, and F.H. Webb, Precise point positioning for the efficient and robust analysis of GPS data from large networks, *Journal of Geophysical Research*, *102* (B3), 5005-5017, 1997.

Zwally, H.J., B. Schutz, W. Abdalati, J. Abshire, C. Bentley, A. Brenner, J. Bufton, J. Dezio, D. Hancock, and D. Harding, ICESat's laser measurements of polar ice, atmosphere, ocean, and land, *Journal of Geodynamics*, *34* (3-4), 405-445, 2002.

Running heading:

ANTARCTIC OCEAN TIDE MODEL VALIDATION

Tables

Table 1: Summary of ocean ocean tide models used in this study

Model	Reference	Latitudinal Limits	Type	Resolution (lat. x long.)
TPXO.2	[*Egbert et al.*, 1994]	80ºS to 70ºN	H + T/P	0.59º x 0.70º
TPXO.6	[*Egbert et al.*, 1994]	86ºS to 90ºN	H + T/P + ERS + T/G	0.25º x 0.25º
CSR3	[*Eanes*, 1994]	78ºS to 90ºN	H + T/P	0.5º x 0.5º
FES95.2	[*Le Provost et al.*, 1998]	86ºS to 90ºN	H + T/P	0.5º x 0.5º
FES99	[*Lefevre et al.*, 2002]	86ºS to 90ºN	H + T/P + TG	0.25º x 0.25º
GOT00.2	[*Ray*, 1999]	86ºS to 90ºN	H+ T/P + ERS	0.5º x 0.5º
NAO.99b	[*Matsumoto et al.*, 2000]	83ºS to 90ºN	H + T/P	0.5º x 0.5º
CADA00.10	[*Padman et al.*, 2002]	86ºS to 58ºS	H + T/P + TG	0.25º x 0.083º
CATS02.01	[*Padman et al.*, 2002]	86ºS to 58ºS	H	0.25º x 0.083º

H – Hydrodynamic model; T/P – TOPEX/Poseidon altimetry data assimilated; ERS – ERS altimetry data assimilated; T/G – Tide Gauge data assimilated

Table 2: GPS-derived ocean tide loading displacement estimates. One standard deviation formal errors are shown in parentheses. No constituents stabilized for sites CONZ, ELHT and ROTH.

Site	N_{days}	*k*	M_2		S_2		N_2		K_2		K_1		O_1		P_1		Q_1	
			A (mm)	*Φ* (°)	*A* (mm)	*Φ* (°)	*A* (mm)	*Φ* (°)	*A* (mm)	*Φ* (°)	*A* (mm)	*Φ* (°)	*A* (mm)	*Φ* (°)	*A* (mm)	*Φ* (°)	*A* (mm)	*Φ* (°)
AMUN	1544	E	0.7 (0.8)	21.5 (61.1)	1.6 (0.8)	-43.3 (27.4)	0.2 (0.8)	6.2 (287.5)	2.2 (0.8)	110.4 (21.3)	0.9 (0.7)	57.2 (43.3)	1.5 (0.7)	145.9 (26.8)	0.8 (0.7)	-163.8 (53.8)	0.3 (0.7)	80.4 (126.9)
		N	1.0 (0.8)	122.1 (48.9)	2.3 (0.8)	148.3 (19.7)	0.2 (0.8)	116.2 (203.7)	2.1 (0.8)	45.4 (21.9)	5.4 (0.7)	-129.1 (7.6)	2.6 (0.7)	-162.7 (15.0)	1.6 (0.7)	-93.9 (24.7)	0.6 (0.7)	-157.1 (63.6)
		U	1.4 (1.3)	25.6 (51.4)	2.3 (1.3)	-9.4 (31.9)	0.5 (1.3)	-28.0 (151.4)	3.8 (1.3)	90.0 (20.6)	3.8 (1.4)	41.8 (21.0)	1.4 (1.4)	-99.0 (60.2)	1.6 (1.4)	7.7 (49.4)	0.7 (1.4)	-144.6 (122.1)
SYOG	2666	E	0.6 (0.5)	-130.7 (46.7)	0.8 (0.5)	-100.9 (34.3)	0.4 (0.5)	159.2 (69.1)	2.2 (0.5)	88.4 (14.4)	2.1 (0.4)	-158.2 (12.5)	1.7 (0.4)	-156.6 (15.7)	1.8 (0.4)	-162.1 (14.0)	0.6 (0.4)	-165.9 (46.7)
		N	1.9 (0.4)	74.0 (13.3)	1.4 (0.4)	99.0 (18.2)	0.4 (0.4)	58.3 (58.5)	2.1 (0.4)	9.3 (13.5)	2.1 (0.3)	-29.2 (9.1)	1.6 (0.3)	-35.3 (12.5)	0.7 (0.3)	38.7 (25.8)	0.2 (0.3)	-30.3 (110.0)
		U	9.5 (1.0)	-94.1 (5.8)	6.2 (1.0)	-75.6 (9.1)	1.8 (1.0)	-94.4 (31.5)	1.7 (1.0)	41.4 (37.1)	8.4 (0.9)	151.8 (6.6)	8.8 (0.9)	134.5 (6.5)	4.3 (0.9)	144.4 (12.3)	2.6 (0.9)	128.9 (21.9)
MAW1	2043	E	1.1 (0.5)	-159.6 (24.1)	1.3 (0.5)	-118.3 (19.5)	0.4 (0.5)	161.3 (75.9)	2.3 (0.5)	-129.4 (12.8)	2.0 (0.4)	-157.5 (14.4)	1.6 (0.5)	-148.5 (17.2)	0.7 (0.5)	-126.4 (35.4)	0.4 (0.5)	-145.3 (70.1)
		N	0.9 (0.4)	143.7 (27.4)	0.2 (0.4)	131.7 (87.5)	0.3 (0.4)	131.7 (87.5)	2.3 (0.4)	122.9 (11.8)	2.0 (0.3)	-44.3 (10.5)	1.4 (0.3)	-58.4 (14.8)	0.3 (0.3)	-143.2 (76.0)	0.3 (0.3)	-106.0 (68.0)
		U	3.7 (0.8)	-27.1 (12.9)	1.8 (0.8)	-154.7 (26.3)	1.5 (0.8)	-31.2 (32.0)	5.1 (0.8)	162.4 (10.6)	7.1 (0.8)	88.1 (6.7)	8.1 (0.8)	97.8 (6.1)	3.3 (0.8)	122.8 (14.0)	2.1 (0.8)	96.9 (23.1)
DAV1	2447	E	0.7 (0.4)	58.0 (34.4)	1.2 (0.4)	-152.1 (20.4)	0.2 (0.4)	3.1 (104.3)	1.3 (0.4)	-153.3 (21.8)	2.1 (0.4)	-174.0 (12.0)	1.4 (0.4)	161.9 (18.2)	0.8 (0.4)	-154.7 (28.9)	0.2 (0.4)	-167.2 (127.7)
		N	1.4 (0.4)	178.5 (15.9)	0.9 (0.4)	-152.9 (25.4)	0.5 (0.4)	161.2 (45.2)	0.8 (0.4)	146.3 (31.7)	2.2 (0.3)	-104.4 (8.7)	1.4 (0.3)	-86.7 (14.2)	0.3 (0.3)	-135.7 (61.4)	0.4 (0.3)	-122.1 (45.7)
		U	6.2 (0.7)	1.2 (6.6)	4.0 (0.7)	114.7 (10.2)	2.1 (0.7)	-27.8 (20.0)	4.7 (0.7)	118.0 (9.8)	8.8 (0.7)	81.3 (4.5)	9.4 (0.7)	80.4 (4.4)	2.8 (0.7)	94.7 (14.0)	2.2 (0.7)	76.8 (19.0)
CAS1	2605	E	1.9 (0.4)	12.6 (12.6)	0.8 (0.4)	24.5 (27.4)	0.8 (0.4)	-3.5 (29.0)	1.3 (0.4)	118.2 (20.2)	0.9 (0.4)	-145.9 (30.9)	1.4 (0.4)	168.9 (18.9)	0.7 (0.4)	-65.3 (35.9)	0.4 (0.4)	167.7 (69.8)
		N	1.6 (0.4)	136.7 (12.7)	1.6 (0.4)	-166.7 (12.8)	0.3 (0.4)	152.5 (60.0)	1.2 (0.4)	62.5 (19.1)	3.5 (0.3)	-122.4 (5.6)	1.5 (0.3)	-133.3 (12.6)	1.2 (0.3)	-125.7 (14.8)	0.5 (0.3)	-125.4 (42.9)
		U	7.9 (0.7)	-34.6 (4.8)	3.2 (0.7)	23.9 (11.7)	2.2 (0.7)	-55.5 (17.3)	2.6 (0.7)	-9.4 (16.8)	11.8 (0.7)	58.6 (3.3)	10.6 (0.6)	47.5 (3.7)	3.7 (0.6)	56.6 (9.8)	2.5 (0.6)	36.4 (15.8)
DUM1	1722	E	1.8 (0.5)	-21.4 (14.7)	1.5 (0.5)	10.0 (17.8)	0.6 (0.5)	-37.2 (43.8)	0.4 (0.5)	-81.3 (70.1)	2.0 (0.5)	170.9 (15.3)	1.2 (0.5)	-177.0 (25.5)	0.9 (0.5)	-148.1 (31.7)	0.3 (0.5)	176.0 (88.8)
		N	1.7 (0.4)	55.1 (13.9)	1.0 (0.4)	124.9 (22.7)	0.4 (0.4)	32.6 (58.4)	1.6 (0.4)	117.7 (16.3)	3.0 (0.4)	-123.4 (8.0)	1.9 (0.4)	-146.8 (12.7)	1.1 (0.4)	-117.3 (20.8)	0.4 (0.4)	-141.0 (62.4)
		U	7.8 (0.9)	-115.7 (6.4)	3.5 (0.9)	-61.4 (14.5)	2.2 (0.9)	-129.3 (23.2)	2.6 (0.9)	-104.7 (20.9)	12.9 (0.9)	35.0 (4.0)	11.0 (0.9)	25.0 (4.8)	3.5 (0.9)	46.0 (14.2)	2.7 (0.9)	10.5 (19.5)
MCM4	2640	E	0.9 (0.5)	-34.9 (29.5)	1.3 (0.5)	-1.3 (21.3)	0.3 (0.5)	-63.9 (95.7)	1.3 (0.5)	-169.6 (24.1)	2.4 (0.4)	163.6 (11.0)	1.9 (0.4)	154.9 (14.1)	0.4 (0.4)	-128.8 (58.3)	0.3 (0.4)	133.0 (87.6)
		N	0.6 (0.5)	79.0 (41.9)	0.5 (0.5)	-24.5 (51.7)	0.3 (0.5)	-13.7 (98.9)	1.4 (0.5)	104.1 (20.9)	3.0 (0.4)	-160.8 (7.5)	1.9 (0.4)	-177.4 (11.5)	1.2 (0.4)	-140.2 (16.8)	0.3 (0.3)	-165.5 (73.0)
		U	2.2 (0.9)	-91.5 (21.8)	0.3 (0.9)	-73.9 (162.0)	0.4 (0.9)	19.4 (136.0)	2.2 (0.9)	88.9 (26.1)	8.7 (0.9)	15.7 (6.0)	8.0 (0.9)	-3.8 (6.8)	2.9 (0.9)	17.1 (17.2)	2.1 (0.9)	-19.7 (25.6)
CONZ	578	E	0.5 (0.6)	-28.4 (67.4)	0.9 (0.6)	-26.9 (41.3)	0.1 (0.6)	-97.3 (253.7)	0.5 (0.6)	117.5 (60.0)	0.8 (0.7)	108.4 (43.1)	0.7 (0.7)	121.3 (54.1)	0.6 (0.7)	139.1 (65.8)	0.2 (0.7)	160.6 (216.6)
		N	0.6 (0.6)	39.9 (60.8)	0.3 (0.6)	85.5 (121.9)	0.2 (0.6)	3.9 (199.2)	0.4 (0.6)	60.2 (83.0)	1.1 (0.6)	-115.8 (33.7)	0.8 (0.6)	-143.3 (43.4)	0.4 (0.6)	-131.8 (81.5)	0.3 (0.6)	-105.6 (104.0)
		U	1.2 (2.4)	-53.2 (116.1)	4.0 (2.5)	-21.0 (36.2)	0.6 (2.4)	54.9 (242.7)	10.4 (2.5)	144.0 (12.1)	7.3 (2.9)	19.5 (19.9)	6.6 (2.7)	2.6 (22.2)	4.7 (2.8)	20.4 (32.8)	0.8 (2.7)	-43.1 (174.6)
ELHT	361	E	1.5 (1.6)	9.6 (63.4)	0.8 (1.6)	3.0 (111.3)	0.4 (1.6)	-31.8 (231.5)	2.8 (1.6)	-130.5 (29.9)	6.5 (1.7)	70.8 (13.7)	2.0 (1.6)	122.0 (43.8)	1.5 (1.6)	-153.2 (61.9)	0.9 (1.6)	95.8 (98.6)
		N	0.7 (1.6)	32.4 (130.0)	0.5 (1.6)	5.1 (169.0)	0.4 (1.6)	-88.5 (203.5)	3.1 (1.5)	129.3 (26.7)	4.1 (1.5)	-39.9 (20.8)	1.1 (1.5)	-142.4 (74.9)	0.9 (1.5)	170.1 (99.8)	0.1 (1.5)	-106.5 (611.7)
		U	2.1 (3.2)	-47.7 (86.2)	2.4 (3.1)	7.4 (75.3)	0.8 (3.1)	-10.3 (220.2)	9.7 (3.1)	168.7 (17.1)	14.8 (3.4)	17.9 (12.4)	9.4 (3.3)	-12.9 (19.2)	4.0 (3.3)	-33.2 (49.1)	3.0 (3.3)	-27.6 (59.4)
ROTH	520	E	2.6 (1.1)	-103.4 (23.6)	2.8 (1.0)	-85.1 (21.3)	0.6 (1.1)	-49.3 (103.4)	2.5 (1.0)	111.9 (21.9)	2.2 (1.0)	-12.4 (22.6)	2.1 (0.9)	-9.5 (24.2)	0.6 (0.9)	13.9 (91.2)	0.5 (0.9)	60.4 (98.1)
		N	1.6 (0.9)	-33.5 (34.2)	1.2 (0.9)	22.9 (43.3)	0.2 (0.9)	-45.9 (223.5)	4.2 (0.9)	21.2 (11.7)	0.9 (0.7)	39.2 (48.4)	1.1 (0.7)	-3.9 (36.7)	0.6 (0.7)	-72.9 (64.5)	0.8 (0.7)	3.8 (47.3)
		U	13.9 (2.1)	71.8 (8.5)	1.7 (2.0)	107.2 (69.1)	3.4 (2.1)	22.5 (34.9)	1.4 (2.0)	85.1 (82.4)	18.2 (1.7)	-109.3 (6.3)	14.9 (1.8)	-129.8 (6.8)	5.0 (1.9)	-109.7 (20.6)	2.2 (1.8)	-154.5 (47.6)
PALM	1707	E	2.9 (0.5)	-104.1 (10.1)	3.1 (0.5)	-98.1 (9.0)	0.5 (0.5)	-95.0 (56.3)	0.2 (0.5)	-82.4 (184.4)	2.1 (0.4)	-28.5 (12.8)	1.7 (0.4)	-18.3 (14.6)	0.8 (0.4)	-53.5 (29.9)	0.2 (0.4)	-16.5 (98.3)
		N	1.7 (0.5)	23.9 (14.6)	1.7 (0.4)	58.0 (15.1)	0.4 (0.5)	-0.2 (59.8)	1.5 (0.4)	63.7 (17.4)	1.1 (0.4)	119.2 (16.3)	0.5 (0.3)	24.3 (38.3)	0.4 (0.3)	136.1 (43.2)	0.2 (0.3)	34.9 (100.1)
		U	18.0 (0.8)	78.8 (2.6)	5.7 (0.8)	125.4 (8.4)	3.0 (0.8)	36.7 (15.9)	1.6 (0.8)	131.4 (29.7)	17.1 (0.8)	-109.1 (2.6)	16.2 (0.7)	-130.5 (2.7)	5.4 (0.7)	-120.1 (7.9)	3.8 (0.7)	-146.5 (11.3)
OHI2	473	E	2.6 (0.7)	-90.0 (16.5)	2.9 (0.7)	-97.0 (13.8)	1.0 (0.7)	-99.9 (44.5)	3.6 (0.7)	-11.7 (9.7)	2.1 (0.6)	-64.0 (18.4)	1.1 (0.6)	-26.0 (28.6)	1.1 (0.6)	-66.5 (33.2)	0.2 (0.6)	33.7 (187.0)
		N	2.0 (0.6)	16.7 (18.9)	2.0 (0.6)	79.9 (17.9)	0.1 (0.6)	8.3 (404.6)	1.7 (0.6)	-84.0 (18.1)	1.7 (0.5)	158.5 (14.4)	0.4 (0.4)	131.2 (54.2)	0.9 (0.5)	154.2 (26.5)	0.3 (0.4)	89.5 (84.5)
		U	24.3 (1.2)	85.6 (3.0)	11.8 (1.2)	128.6 (6.0)	4.1 (1.3)	68.3 (17.4)	2.5 (1.2)	-138.4 (25.5)	16.4 (1.1)	-120.5 (3.9)	17.9 (1.1)	-133.8 (3.3)	5.6 (1.1)	-119.8 (11.5)	4.1 (1.1)	-150.6 (14.5)
OHIG	1679	E	2.0 (0.5)	-92.5 (14.7)	2.4 (0.5)	-99.3 (12.6)	0.5 (0.5)	-38.6 (59.5)	2.7 (0.5)	86.4 (13.8)	2.3 (0.5)	-48.0 (13.3)	1.7 (0.5)	-14.6 (19.1)	0.8 (0.5)	19.6 (35.4)	0.2 (0.5)	29.7 (135.2)
		N	2.7 (0.5)	6.8 (9.4)	1.7 (0.5)	75.0 (15.7)	0.8 (0.5)	-31.5 (33.3)	2.2 (0.4)	12.0 (14.9)	0.8 (0.4)	158.6 (24.9)	0.3 (0.3)	72.8 (77.6)	0.1 (0.4)	48.0 (147.7)	0.1 (0.3)	-62.0 (315.9)
		U	22.9 (1.0)	85.9 (2.5)	11.8 (1.0)	123.0 (4.9)	3.2 (1.0)	59.4 (18.1)	0.5 (1.0)	-169.0 (151.3)	16.0 (0.9)	-120.3 (3.6)	16.5 (0.9)	-136.0 (3.6)	5.3 (0.9)	-117.5 (9.9)	3.8 (0.9)	-153.5 (15.6)
BELG	1200	E	1.9 (0.7)	130.5 (20.0)	0.7 (0.6)	126.2 (54.8)	0.6 (0.7)	126.8 (64.1)	1.1 (0.6)	-77.5 (37.0)	1.1 (0.5)	-49.1 (28.9)	1.4 (0.5)	-121.0 (21.3)	0.7 (0.5)	-163.7 (42.4)	0.5 (0.5)	-148.1 (60.2)
		N	4.4 (0.7)	-118.3 (8.6)	3.4 (0.6)	-93.2 (10.6)	0.4 (0.7)	-136.2 (92.8)	1.8 (0.6)	-160.4 (20.8)	3.9 (0.5)	21.4 (7.1)	2.9 (0.5)	15.3 (9.5)	1.4 (0.5)	30.1 (19.6)	0.6 (0.5)	-4.1 (42.7)
		U	13.3 (1.2)	80.2 (5.1)	7.0 (1.2)	101.2 (9.7)	2.3 (1.2)	58.3 (30.6)	1.8 (1.2)	165.8 (38.6)	9.7 (1.2)	-137.9 (6.9)	11.0 (1.2)	-157.8 (6.3)	3.1 (1.2)	-149.6 (21.7)	2.5 (1.2)	-174.0 (27.7)
VESL	1496	E	2.5 (0.6)	77.0 (14.3)	2.4 (0.6)	96.7 (14.3)	0.6 (0.6)	18.0 (57.5)	5.6 (0.6)	77.3 (6.7)	2.2 (0.5)	-129.0 (13.3)	1.5 (0.5)	-114.9 (19.1)	0.9 (0.5)	-112.6 (29.6)	0.5 (0.5)	-99.1 (59.9)
		N	0.9 (0.6)	-141.9 (36.5)	0.9 (0.6)	-79.2 (37.4)	0.6 (0.6)	-119.6 (60.4)	4.3 (0.6)	-23.9 (8.1)	2.3 (0.4)	20.4 (10.4)	2.1 (0.4)	0.9 (11.3)	1.4 (0.4)	30.6 (16.9)	0.4 (0.4)	-29.0 (53.5)
		U	4.3 (1.1)	8.1 (14.6)	5.0 (1.1)	24.5 (12.7)	0.7 (1.1)	-61.1 (88.0)	5.9 (1.1)	27.2 (11.8)	3.1 (1.0)	139.6 (19.7)	8.6 (1.0)	174.8 (7.2)	2.4 (1.0)	179.0 (24.8)	2.2 (1.0)	178.3 (28.7)

Table 3: Smallest misfit S^2 between GPS and model estimates of ocean tide loading displacement (omitting K_1 and K_2) for the three-dimensional and vertical-only cases, with one standard deviation formal errors. The corresponding model is also shown.

Site	Three-dimensional misfit		Vertical misfit	
	Smallest S^2 (mm^2)	Corresponding Model	Smallest S^2 (mm^2)	Corresponding Model
AMUN	14.2±8.4	FES95.2	5.9±6.6	FES95.2
SYOG	22.7±7.5	CATS02.01	13.8±7.0	CATS02.01
MAW1	8.1±4.2	CADA00.10	4.3±3.3	CADA00.10
DAV1	3.6±2.5	TPXO.6	1.7±1.8	TPXO.6
CAS1	7.5±2.4	TPXO.6	1.2±1.4	TPXO.6
DUM1	7.1±3.6	TPXO.6	3.1±3.1	CATS02.01
MCM4	12.5±5.0	TPXO.6	3.8±3.4	TPXO.6
CONZ	32.7±26.9	GOT00.2	26.8±26.7	GOT00.2
ELHT	35.8±33.4	TPXO.6	24.0±32.3	TPXO.6
ROTH	8.5±8.4	TPXO.6	3.6±7.4	TPXO.6
PALM	14.3±5.1	FES99	5.8±3.9	FES99
OHI2	13.8±7.8	FES99	9.8±7.5	FES99
OHIG	8.6±4.5	CADA00.10	3.6±3.7	CADA00.10
BELG	11.8±6.6	TPXO.6	2.6±3.8	FES99
VESL	7.7±5.0	FES95.2	3.5±4.1	TPXO.6

Table 4: AMUN gravity vector differences and S^2 (in μGal and μGal^2, respectively), ordered by ascending S^2.

Models	Tidal Constituents								S^2
	M_2	S_2	N_2	K_2	K_1	O_1	P_1	Q_1	
TPXO.6	0.055	0.017	0.024	0.016	0.042	0.041	0.027	0.014	0.009
CADA00.10	0.085	0.039	0.046	0.049	0.021	0.039	0.035	0.007	0.015
FES99	0.014	0.034	0.071	0.025	0.045	0.078	0.027	0.020	0.016
CATS02.01	0.096	0.058	0.026	0.037	0.044	0.030	0.035	0.010	0.018
FES95.2	0.100	0.128	0.017	0.037	0.083	0.083	0.027	0.046	0.045
GOT00.2	0.118	0.056	0.043	0.052	0.008	0.176	0.013	0.046	0.055
TPXO.2	0.269	0.179	0.046	0.046	0.145	0.137	0.039	0.031	0.150
CSR3	0.273	0.137	0.015	0.027	0.188	0.276	0.055	0.054	0.212
NAO.99b	0.366	0.213	0.091	0.064	0.255	0.193	0.064	0.052	0.300

Figures

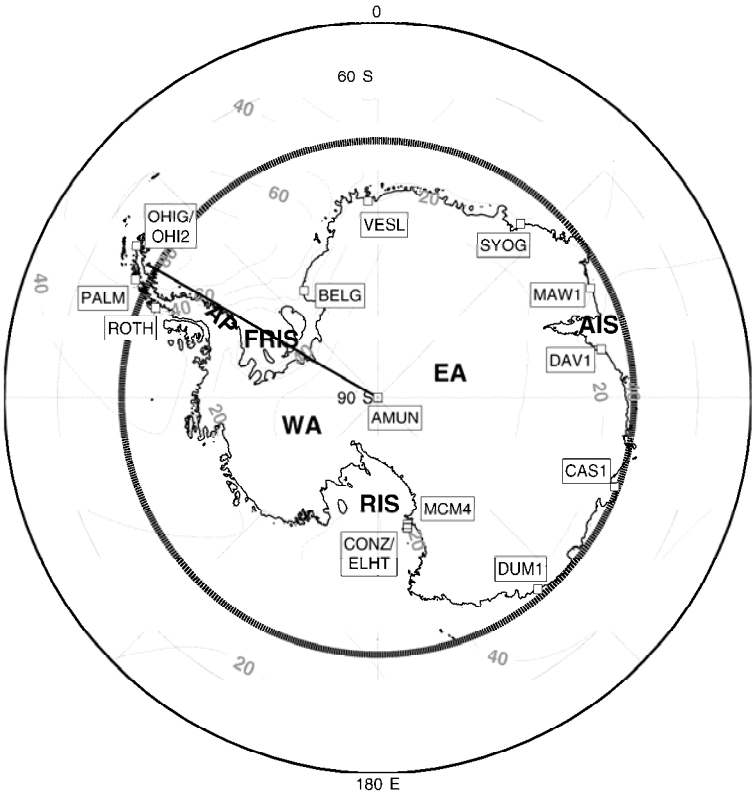

Figure 1: Location map of the GPS sites used in this study. The contours represent (in mm) the approximate maximum magnitude (σ_{max}) of vertical ocean tide loading displacement using CATS02.01 supplemented by TPXO.6. EA is East Antarctica, WA is West Antarctica, AP is the Antarctic Peninsula, FRIS is the Filchner-Ronne Ice Shelf, RIS is the Ross Ice Shelf and AIS is the Amery Ice Shelf. The thick, solid line shows the profile which forms the basis of Figure 3. The thick dashed line shows the 66°S latitude, the approximate T/P southern limit.

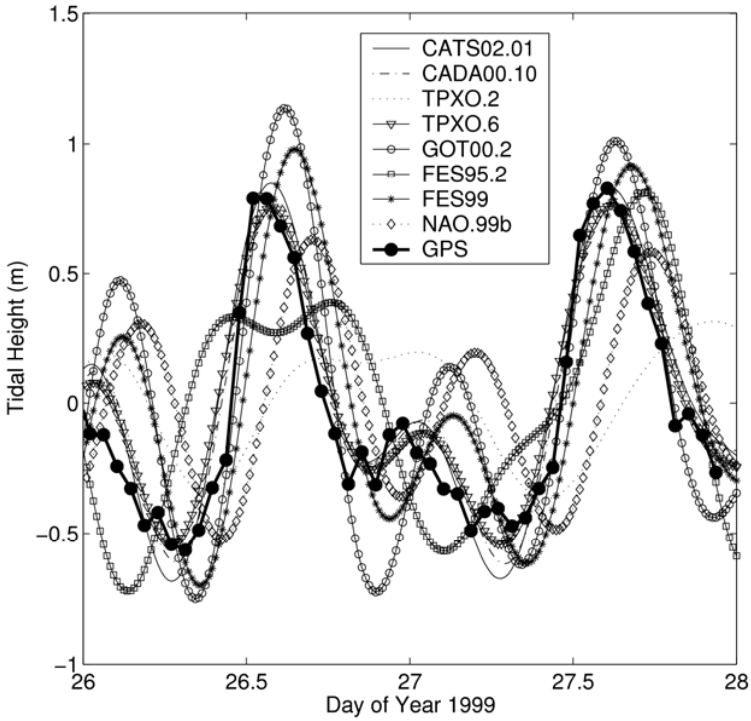

Figure 2: Ocean tide heights for a location on the Amery Ice Shelf from several ocean tide models compared with GPS measurements. The GPS heights were determined using the GAMIT software [*King and Bock*, 2001] using a 1 hr static window processing methodology, relative to reference sites located onshore. The GPS height precision is approximately 0.05 m. An estimate from the CSR3 model is not shown since this location is outside the model domain. Mean values have been removed from each data set.

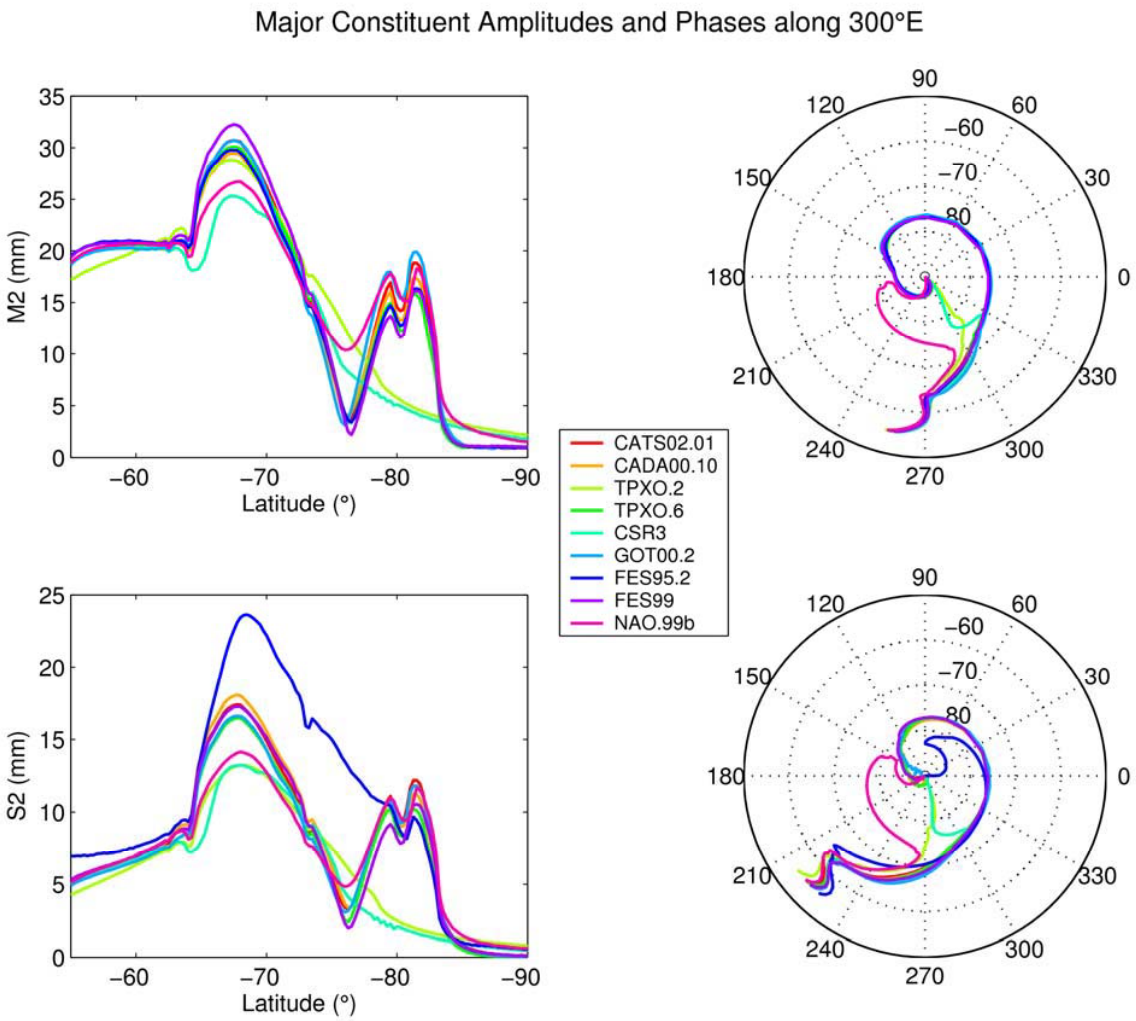

Figure 3: Estimates of ocean tide loading displacement amplitudes and phase lags based on ocean tide models for the two most energetic constituents along the 300° longitude profile from 55°S to the South Pole shown in Figure 1.

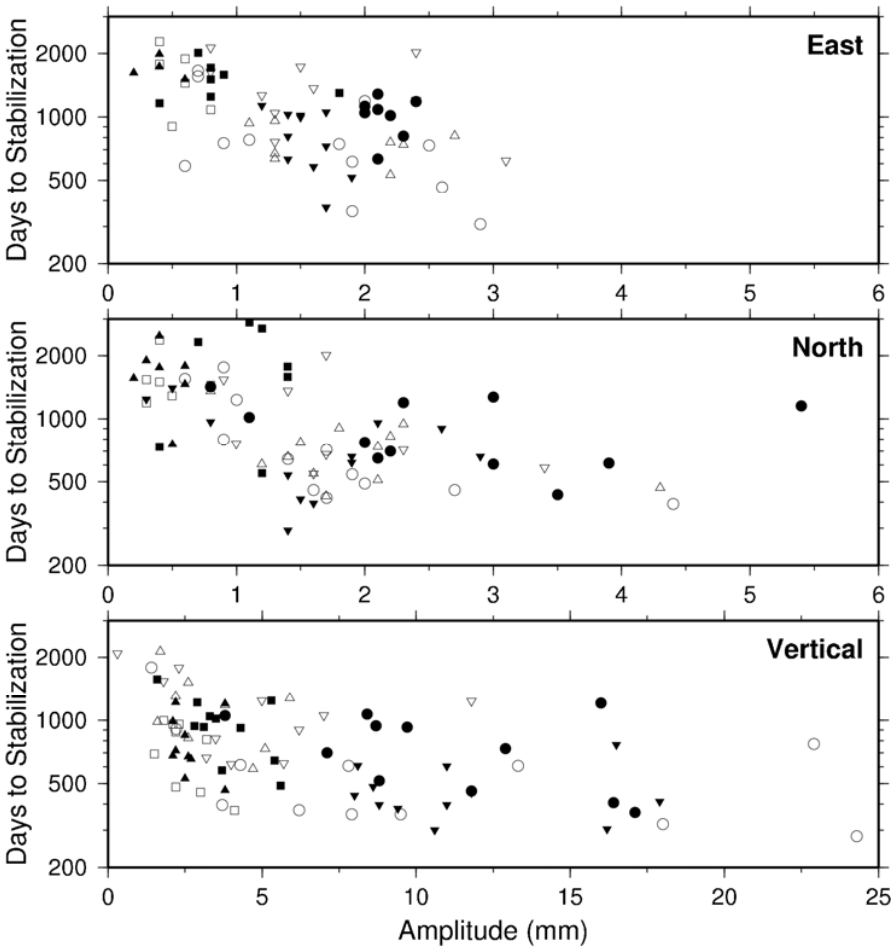

Figure 4: Number of daily solutions required for constituents to stabilize. Open symbols: M_2 (circle); S_2 (inverted triangle); N_2 (square); K_2 (triangle). Filled symbols: K_1 (circle); O_1 (inverted triangle); P_1 (square); Q_1 (triangle). Note that stabilization time is shown on a log scale.

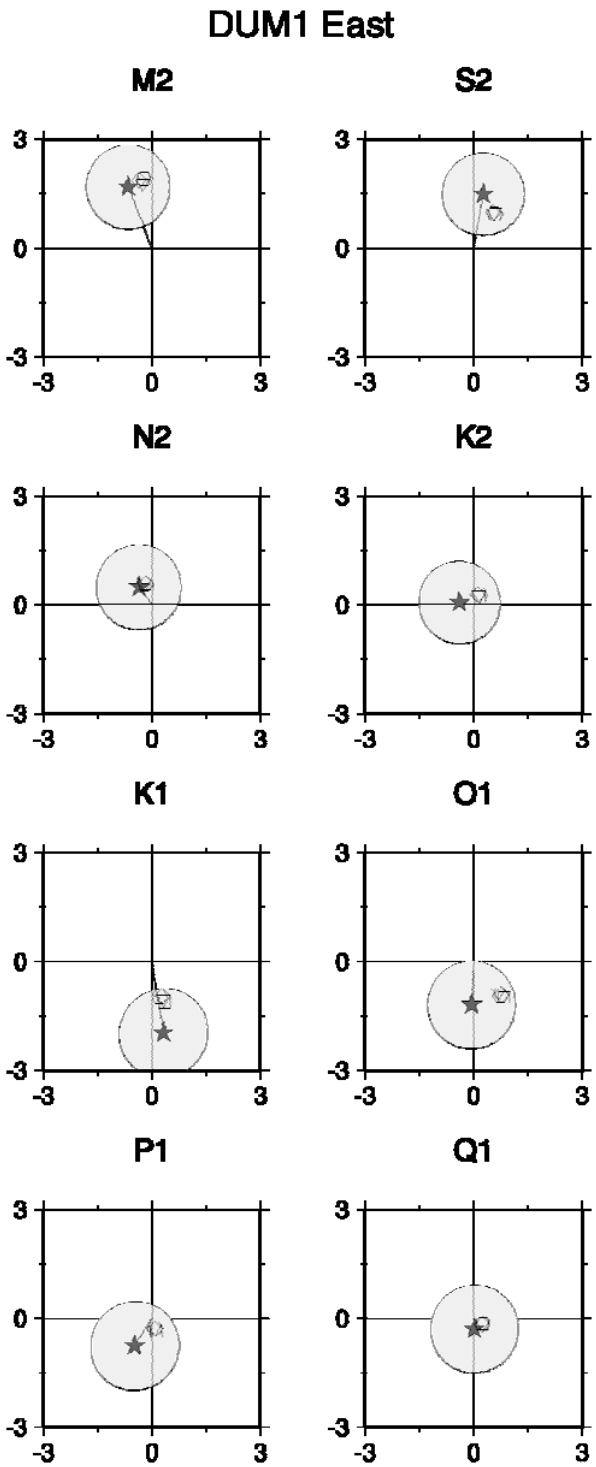

Figure 5: Phasor diagrams of eastward ocean tide loading displacement at DUM1 from GPS and models (in mm). The GPS estimates are represented by filled stars along with their error ellipse (95% confidence interval). Representative model estimates (TPXO.2, diamond; TPXO.6, hexagon; FES99, triangle; CATS02.01, square) are also shown.

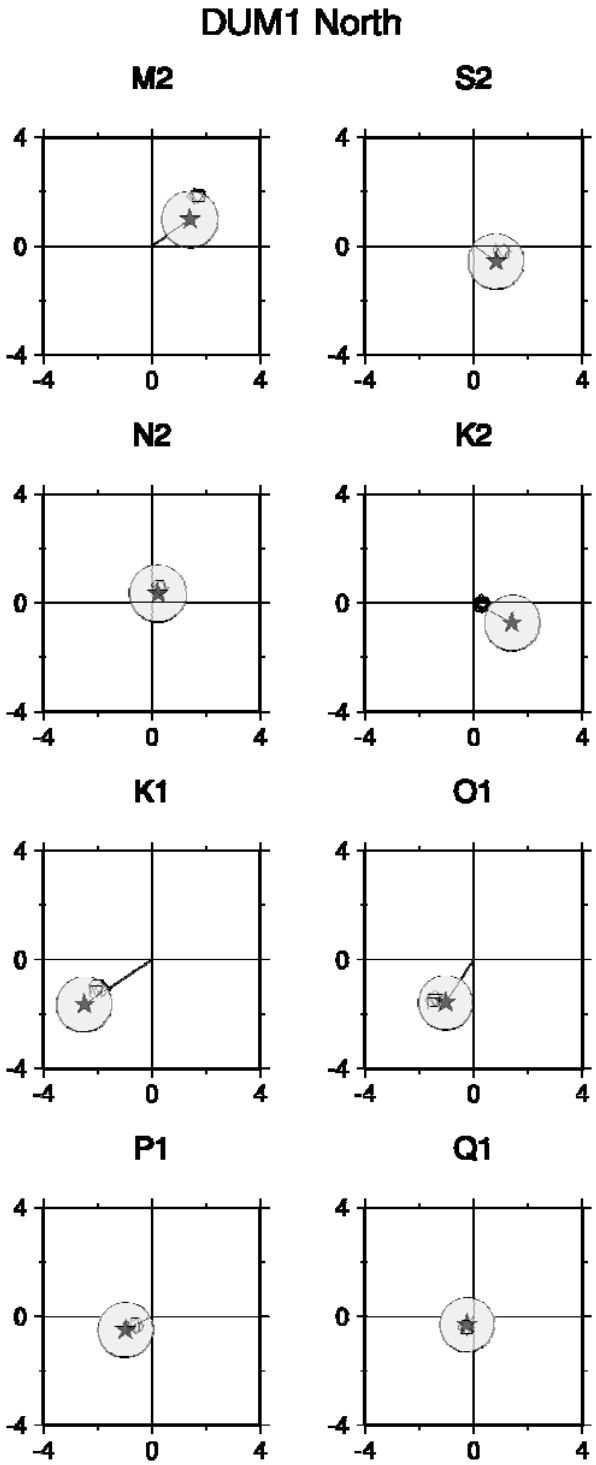

Figure 6: Phasor diagrams of northward ocean tide loading displacement at DUM1 from GPS and models (in mm). The symbols are as for Figure 4.

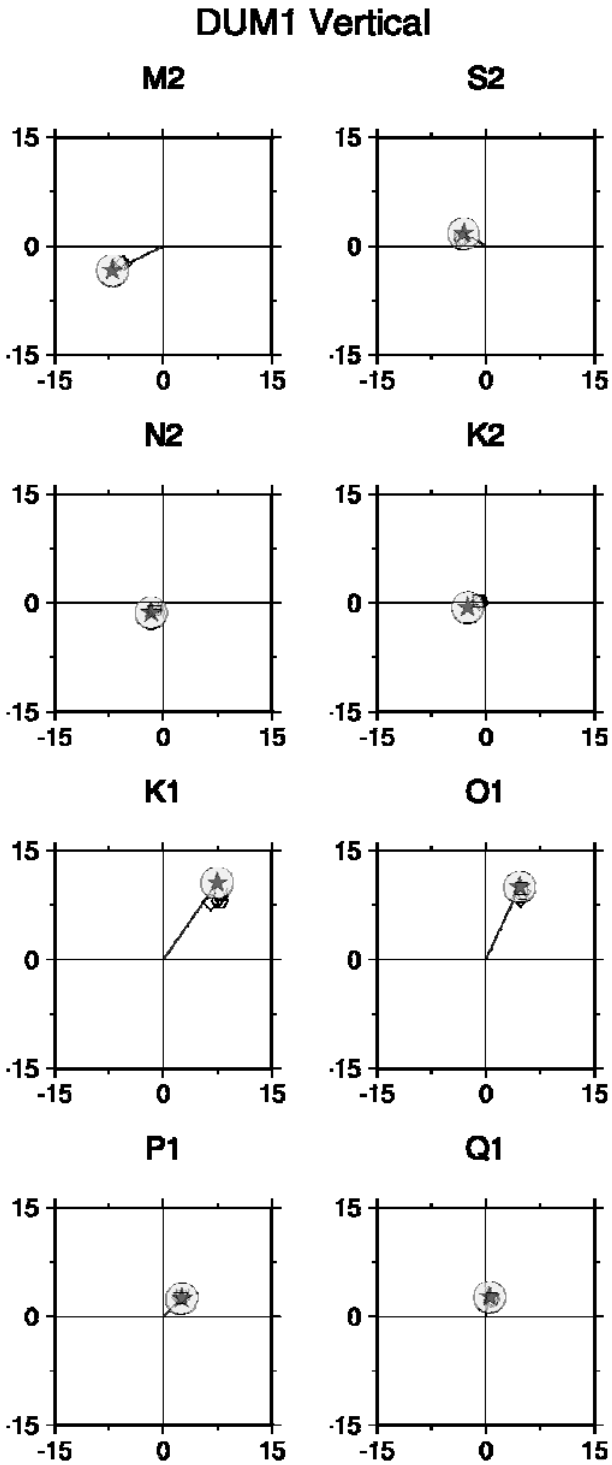

Figure 7: Phasor diagrams of vertical ocean tide loading displacement at DUM1 from GPS and models (in mm). The symbols are as for Figure 4.

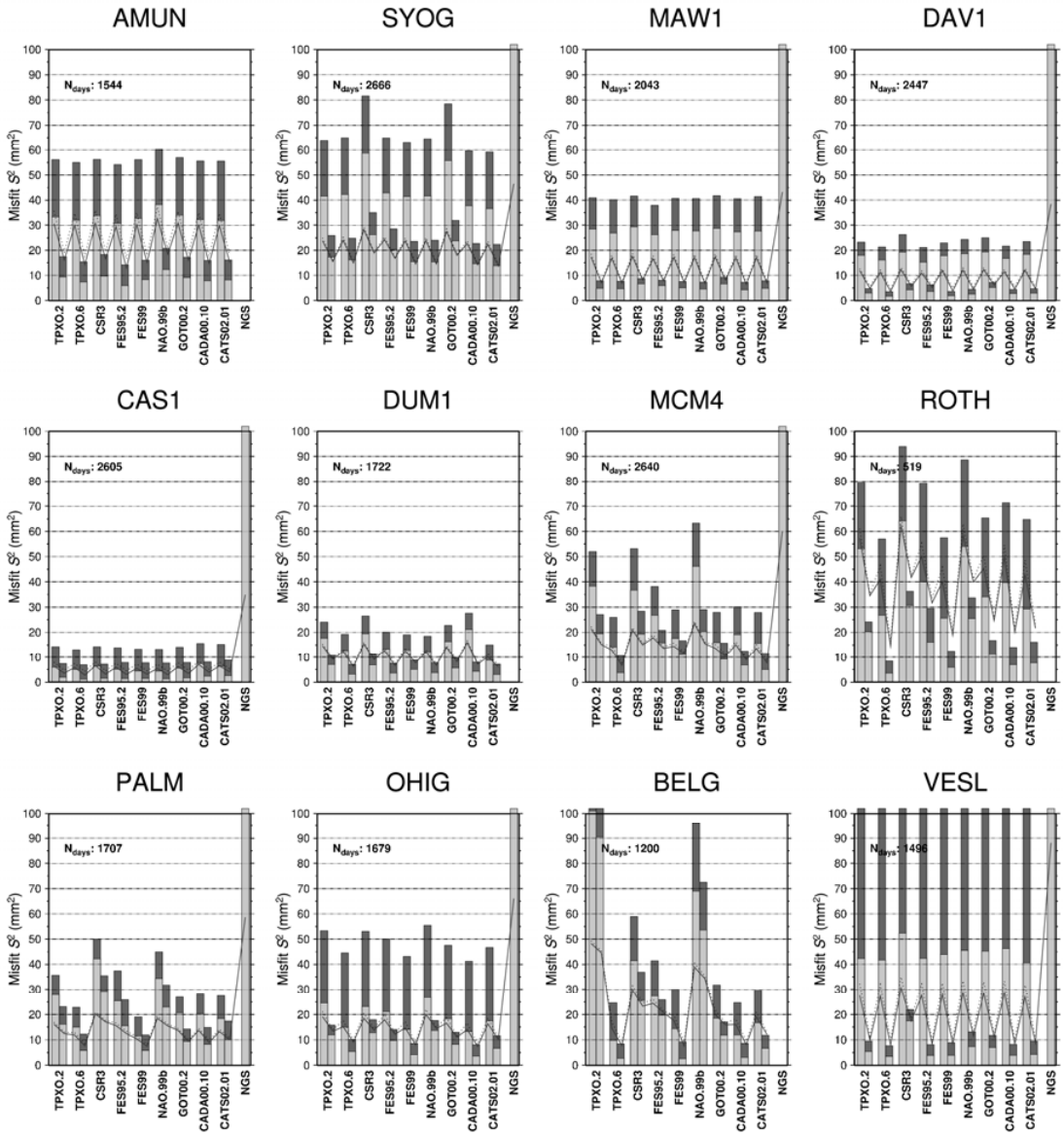

Figure 8: Misfit (S^2) of the GPS and model ocean tide loading displacement estimates (in mm^2) with sites ordered by increasing longitude. The left hand bar shows the misfit for all constituents and the right hand bar has both K_1 and K_2 omitted. The dark grey bar is the three-dimensional misfit and the light grey bar is the vertical-only misfit. NGS refers to the misfit of our GPS results with those of *Schenewerk et al.* [2001]. Misfits >100 mm^2 are capped at just greater than 100 mm^2. The solid and dotted lines represents the 95% confidence interval for the vertical and three-dimensional misfits respectively.

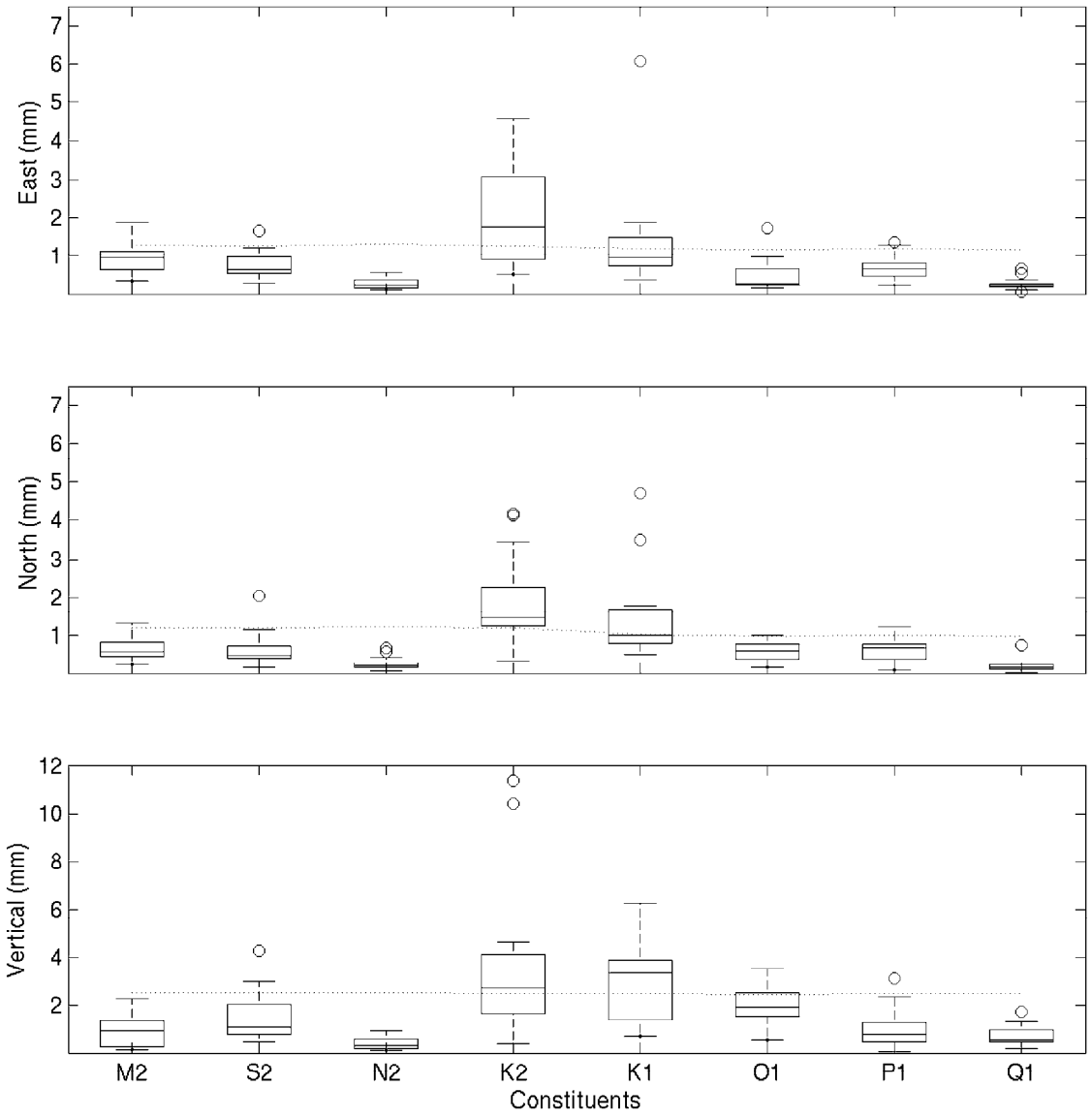

Figure 9: Box-and-whisker plot of the residual vector amplitudes per constituent using TPXO.6. The box describes the lower and upper quartiles and the line within the box describes the median. The whiskers represent 1.5 times the inter quartile range and the open circle symbols represent data points outside these values. Different scales have been used for the horizontal and vertical constituent axes. The dotted lines represent the formal errors (95% confidence interval).

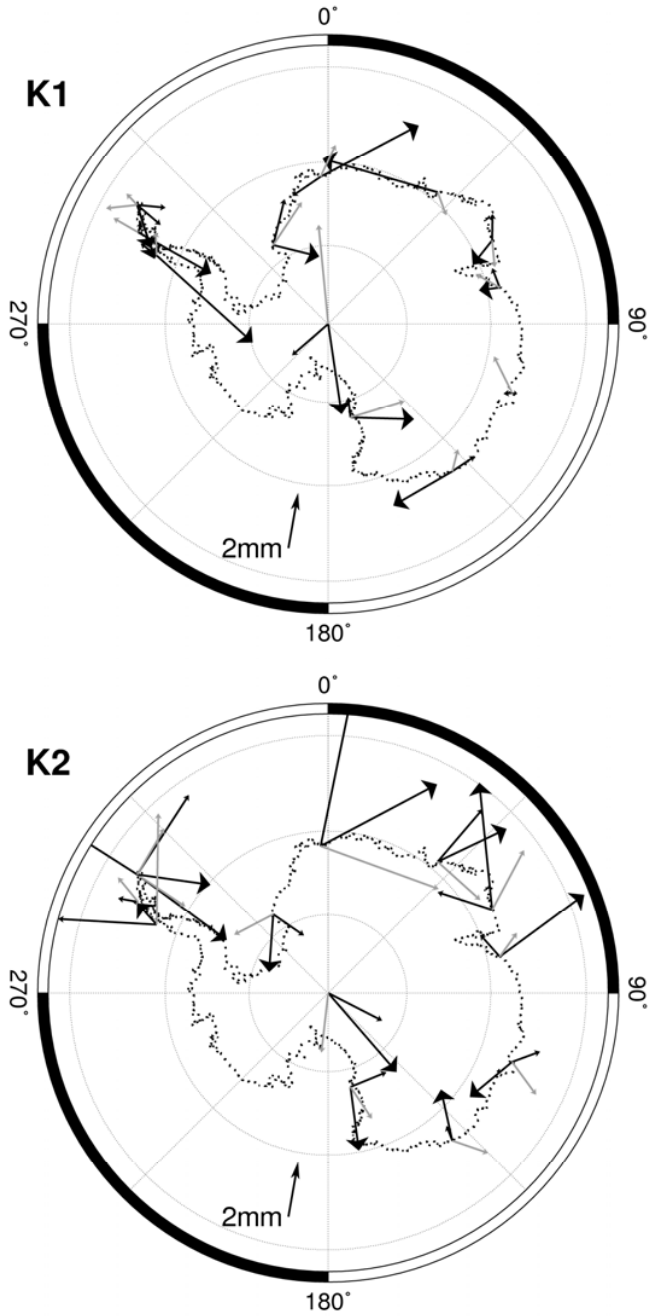

Figure 10: Phasor plots of the K_1 and K_2 ocean tide loading displacement residuals following the removal of the TPXO.6 model estimate, for each of the east (black arrow, small head), north (grey arrow) and vertical (black arrow, large head) components. Local north at each site is 0° phase.

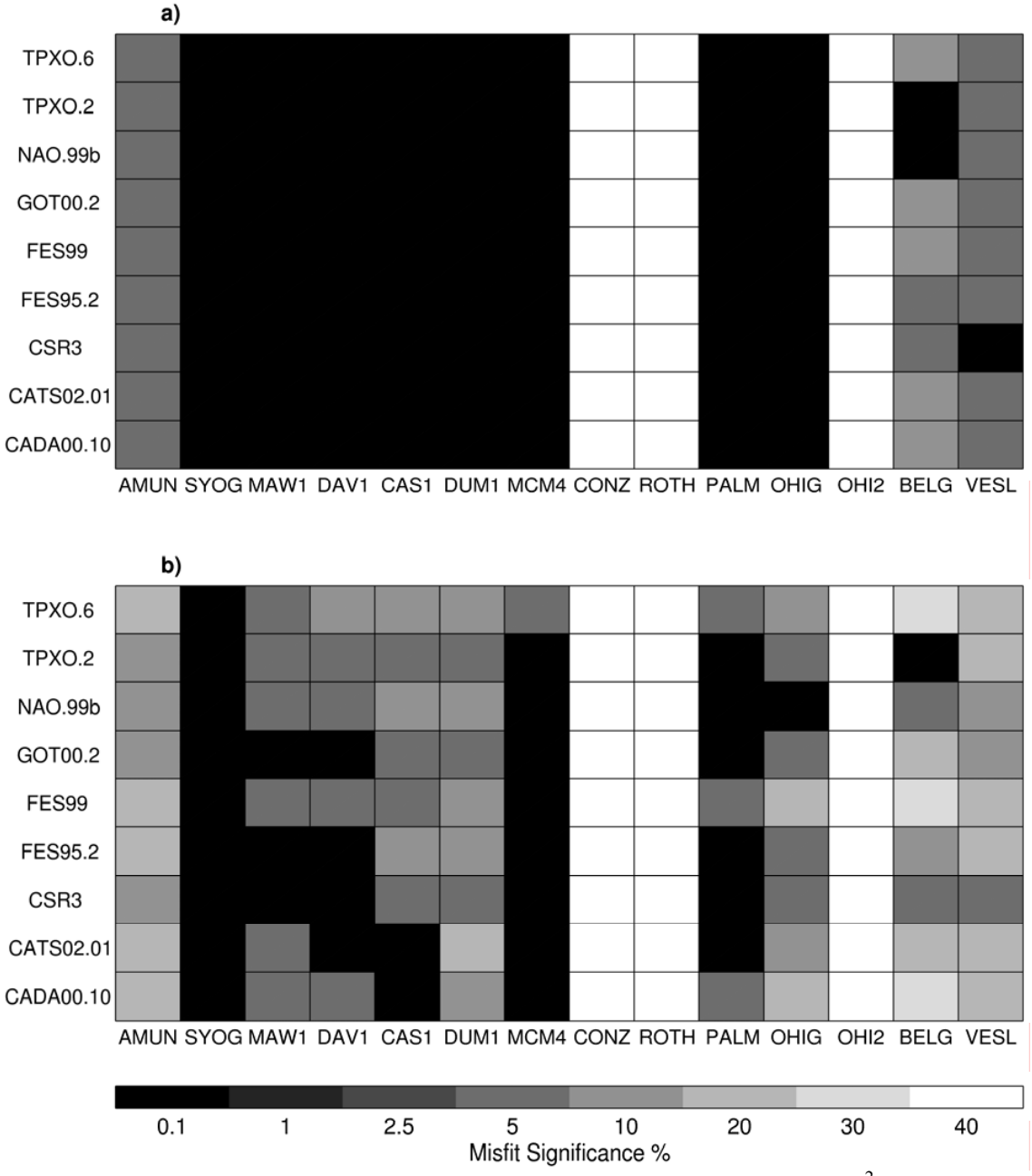

Figure 11: Significance of the three-dimensional (a) and vertical-only misfits S^2 at each of the sites using the various ocean tide models. Lower percentages (dark grey shades) reflect increased likelihood that the misfits are significant and vice versa.

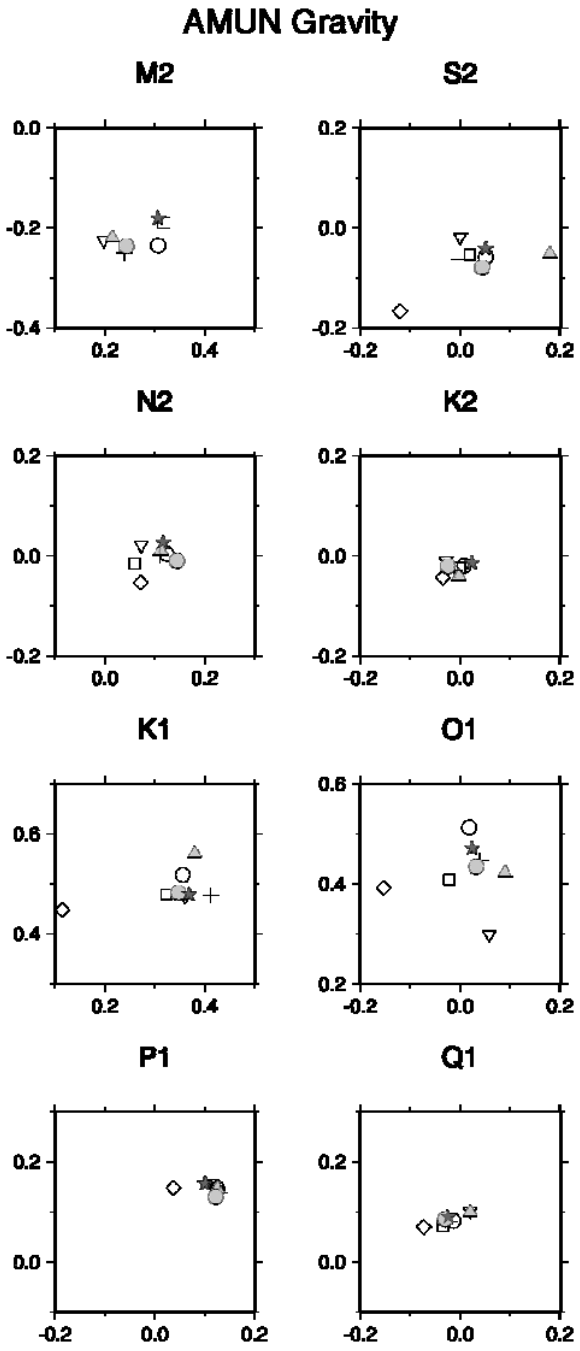

Figure 12: Phasor diagrams of gravity tidal variations at AMUN (in μGal). The gravity estimate is represented by a filled star. Representative model estimates (TPXO.6, unfilled circle; NAO.99b, diamond; GOT00.2, inverted triangle; FES99, square; FES95.2, filled triangle; CATS02.01, cross; CADA00.10, filled circle) are also shown. All sub-figures are at the same scale.

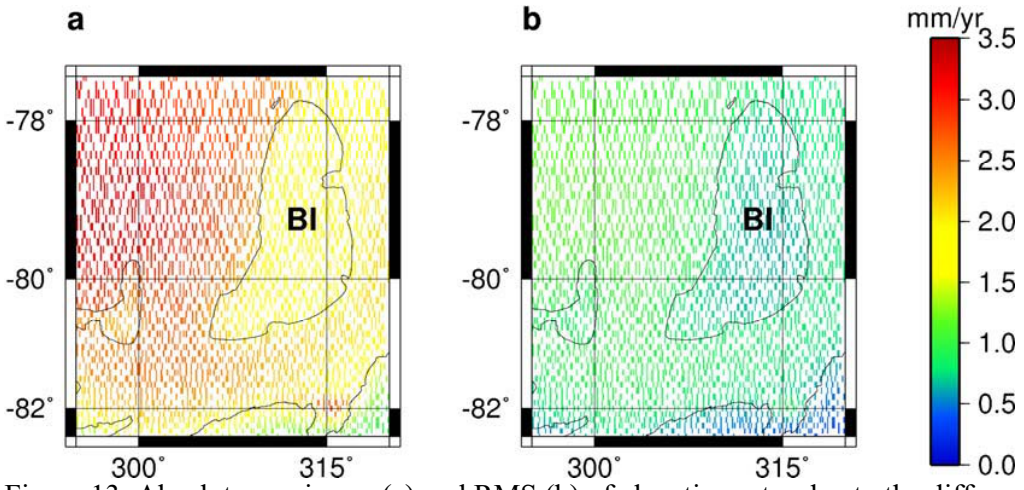

Figure 13: Absolute maximum (a) and RMS (b) of elevation rates due to the difference between ocean tide loading displacement estimates from GOT00.2 and FES99. BI is Berkner Island.